J. Fluid Mech. (2019), *vol.* 873, *pp.* 410–440.
doi:10.1017/jfm.2019.413

Turbulent flow of finite-size spherical particles in channels with viscous hyper-elastic walls

M. N. Ardekani[1,†], **M. E. Rosti**[1] **and L. Brandt**[1]

[1]Linné Flow Centre and SeRC (Swedish e-Science Research Centre), KTH Mechanics, SE-100 44 Stockholm, Sweden

(Received 12 December 2018; revised 14 May 2019; accepted 15 May 2019; first published online 24 June 2019)

We study single-phase and particle-laden turbulent channel flows bounded by two incompressible hyper-elastic walls with different deformability at bulk Reynolds number 5600. The solid volume fraction of finite-size neutrally buoyant rigid spherical particles considered is 10 %. The elastic walls are assumed to be of a neo-Hookean material. A fully Eulerian formulation is employed to model the elastic walls together with a direct-forcing immersed boundary method for the coupling between the fluid and the particles. The data show a significant drag increase and the enhancement of the turbulence activity with growing wall elasticity for both the single-phase and particle-laden flows when compared with the single-phase flow over rigid walls. Drag reduction and turbulence attenuation is obtained, on the other hand, with highly elastic walls when comparing the particle-laden flow with the single-phase flow for the same wall properties; the opposite effect, drag increase, is observed upon adding particles to the flow over less elastic walls. This is explained by investigating the near-wall turbulence, where the strong asymmetry in the magnitude of the wall-normal velocity fluctuations (favouring positive v'), is found to push the particles towards the channel centre. The particle layer close to the wall contributes to turbulence production by increasing the wall-normal velocity fluctuations, so that in the absence of this layer, smaller wall deformations and in turn turbulence attenuation is observed. For a moderate wall elasticity, we increase the particle volume fraction up to 20 % and find that particle migration away from the wall is the cause of turbulence attenuation with respect to the flow over rigid walls. However, for this higher volume fractions, the particle induced stress compensates for the decreasing Reynolds shear stress, resulting in a higher overall drag for the case with elastic walls. The effect of the wall elasticity on the overall drag reduces significantly with increasing particle volume fraction.

Key words: multiphase flow, particle/fluid flows

1. Introduction

Interaction of elastic structures with multiphase flows is of utmost importance in different fields of science and technology, ranging from biological applications (Freund 2014) to energy harvesting (McKinney & DeLaurier 1981). Materials for which the constitutive behaviour is only a function of the current state of deformation

† Email address for correspondence: mehd@mech.kth.se

are generally known as elastic. When the work done by the stresses during the object deformation is function only of the initial and final configurations, the behaviour of the material is path independent and a stored strain energy function or elastic potential can be defined (Bonet & Wood 1997). These so-called hyper-elastic materials show nonlinear stress–strain curves and are generally used to describe rubber-like materials. The aim of this work is to gain fundamental understanding of the interaction between the particle-laden turbulent flow and hyper-elastic walls.

1.1. *Turbulent channel flow of finite-size particles*

Suspensions of solid particles are relevant in many environmental and industrial processes (Guazzelli & Morris 2011) such as sediment transport in estuaries (Mehta 2014), blood flow in the human body, pyroclastic flows and pulp fibres in the paper making industry (Lundell, Söderberg & Alfredsson 2011).

The first simulations of finite-size particles in a turbulent channel flow were performed by Pan & Banerjee (1996). These authors revealed that turbulent fluctuations and stresses increase in the presence of the solid phase. Matas, Morris & Guazzelli (2003), Loisel *et al.* (2013), Yu *et al.* (2013) reported a decrease of the critical Reynolds number for transition to turbulence in the semi-dilute regime with neutrally buoyant spherical particles. The simulations by Shao, Wu & Yu (2012) revealed a decrease of the fluid streamwise velocity fluctuations due to an attenuation of the large-scale streamwise vortices in a turbulent channel flow. Indeed, when the Reynolds number is sufficiently high, the flow becomes turbulent, with chaotic and multi-scale dynamics. In this regime, the presence of particles in the flow can alter the turbulent structures (Naso & Prosperetti 2010; Vreman 2015; Gualtieri, Battista & Casciola 2017), leading to turbulence modulation at large enough volume fractions (Lucci, Ferrante & Elghobashi 2010; Tanaka & Teramoto 2015). Lashgari *et al.* (2014, 2016) documented the existence of three different regimes when changing the volume fraction ϕ of neutrally buoyant spherical particles and the Reynolds number Re: a laminar-like regime at low Re and low to intermediate ϕ where the viscous stress dominates the total dissipation, a turbulent-like regime at high Reynolds number and low to intermediate ϕ where the turbulent Reynolds stress plays the main role in the momentum transfer across the channel and a third regime at higher ϕ, denoted as inertial shear thickening, characterized by a significant enhancement of the wall shear stress due to particle-induced stresses. Picano, Breugem & Brandt (2015) investigated dense suspensions in turbulent channel flow up to a volume fraction of 20 %. Their study revealed that the overall drag increase is due to the enhancement of the turbulence activity up to a certain volume fraction ($\phi \leqslant 10\,\%$) and to significant particle-induced stresses at higher concentrations. Costa *et al.* (2016) explained that the turbulent drag of sphere suspensions is always higher than what predicted by only accounting for the effective suspension viscosity. They attributed this increase to the formation of a particle-wall layer, a layer of spheres forming near the wall in turbulent suspensions. Based on the thickness of the particle-wall layer, they proposed a relation able to predict the friction Reynolds number as a function of the bulk Reynolds number. Indeed, the particle-wall layer has been found to have a significant effect on the modulation of the near-wall turbulence, as confirmed in the case of non-spherical particles (Ardekani *et al.* 2017; Eshghinejadfard, Hosseini & Thévenin 2017; Ardekani & Brandt 2019) where the absence of this layer leads to attenuation of the turbulence activity, resulting in drag reduction. Picano *et al.* (2015) attribute the formation of the near-wall layer of spherical particles to the

strong wall–particle lubrication interaction that stabilizes the particle wall-normal position, forcing it to roll on the wall. As a consequence, a complex wall might change the particle dynamics in this region, affecting the formation of this layer. Motivated by this, we study here the effect of hyper-elastic walls on the formation of the particle-wall layer and on the near-wall multi-phase turbulence.

1.2. *Flow over deformable compliant surfaces*

Many applications involve flow over complex walls that cannot be assumed to be smooth flat surfaces. The study of the flow over these complex walls can be dated back to the pioneering work of Nikuradse (1933, 1950), who presented a large number of experimental measurements in pipes with walls covered by sand grains. Many studies have been performed since then on the turbulent flow over rough surfaces (Antonia & Krogstad 2001; Cabal, Szumbarski & Floryan 2002; Belcher, Jerram & Hunt 2003; Leonardi *et al.* 2003, 2004) as well as over porous walls (Beavers, Sparrow & Magnuson 1970; Breugem, Boersma & Uittenbogaard 2006; Tilton & Cortelezzi 2006; Suga *et al.* 2010; Rosti, Cortelezzi & Quadrio 2015). These have shown the destabilizing effect of the wall on the flow, the disruption of the high- and low-speed streaks close to the wall and increased wall-normal velocity fluctuations at the interface.

The two-way coupling between the flow and the dynamics of a deformable wall distinguishes these types of walls from the above-mentioned complex rigid surfaces (e.g. rough and permeable walls). This coupling allows for non-zero wall-normal velocities at the interface, due to the wall movement. The early experimental studies of Lahav, Eliezer & Silberberg (1973), Krindel & Silberberg (1979) showed a significant decrease of the critical Reynolds number for transition to turbulence of the flow in gel-coated tubes. Several studies have been then devoted to the linear stability of the fluid flow through channels and pipes with elastic and hyper-elastic walls (Kumaran 1995; Srivatsan & Kumaran 1997; Kumaran 1998*a*,*b*; Kumaran & Muralikrishnan 2000), reporting the possibility of the flow being unstable even in the absence of fluid inertia. These authors attribute the instabilities to the energy transfer from the mean flow to the fluctuations due to the deformation work at the interface (Shankar & Kumaran 1999).

The effect of elastic surfaces on a fully developed turbulent flow has been more seldom considered in the literature. Luo & Bewley (2003, 2005) considered a new class of compliant surfaces, called tensegrity fabrics: a pre-tensioned network of compressive members interconnected by tensile ones. These authors reported a large drag increase and a turbulence activity enhancement, following a resonating condition between the wall deformation and the turbulent flow. Recently, Rosti & Brandt (2017) performed the first direct numerical simulations of turbulent channel flow, bounded by an incompressible hyper-elastic wall. Their study revealed that the skin friction increases monotonically with the material elastic modulus, while the turbulent flow is affected by the moving wall even at low values of elasticity. These authors show how the elasticity is the key parameter determining the turbulent flow modulation and the wall deformation.

As concerns multiphase flows, several recent studies consider a single object interacting with a soft wall (Skotheim & Mahadevan 2004; Salez & Mahadevan 2015; Saintyves *et al.* 2016; Rallabandi *et al.* 2017), while there is no study in the literature on the suspensions of rigid particles in a channel flow with elastic walls. Therefore, in this study, we investigate the effect of wall elasticity on the particles dynamics and document the resulting alterations in the transport properties of the suspension.

1.3. *Outline*

In this work, we present the first direct numerical simulations of turbulent channel flow with hyper-elastic walls laden with finite-size rigid spherical particles. The governing equations and the flow geometry are introduced in § 2, followed by the results of the numerical simulations in section § 3. The main conclusions are finally drawn in § 4.

2. Methodology

In this work we study the turbulent flow of an incompressible viscous fluid through a channel with incompressible hyper-elastic walls, laden with non-Brownian neutrally buoyant finite-size rigid spherical particles. To this purpose, the numerical method in Sugiyama *et al.* (2011), Rosti & Brandt (2017) based on a fully Eulerian formulation is employed to account for the fluid–structure interaction at the interfaces ; this is combined with a direct-forcing immersed boundary method (IBM) (Uhlmann 2005; Breugem 2012) to model the coupling between the fluid and the particles. The IBM is complemented by lubrication, friction and collision models for short-range particle–particle interactions (Costa *et al.* 2015; Ardekani *et al.* 2016), while a sub-grid force (Bolotnov *et al.* 2011; De Vita *et al.* 2019) is used to model the particle–interface interactions (interactions between the solid spheres and the elastic walls). A brief description of the numerical method is given below in § 2.1.

2.1. *Governing equations & the numerical scheme*

For the fluid–structure interaction at the interface, we use the so called one-continuum formulation (Tryggvason, Sussman & Hussaini 2007), solving only one set of equations for the conservation of momentum and the incompressibility constraint in the fluid phase and the elastic layer,

$$\partial_t u_i + \partial_j u_i u_j = \frac{1}{\rho}\partial_j \sigma_{ij}, \tag{2.1}$$

$$\partial_i u_i = 0. \tag{2.2}$$

Here, u_i is a monolithic velocity vector field, volume averaged (Quintard & Whitaker 1994) between the fluid phase and the elastic layer across the interface and ρ is the density, assumed to be the same in both phases. Using a volume of fluid (VoF) approach (Hirt & Nichols 1981; Rosti & Brandt 2017), the Cauchy stress tensor $\boldsymbol{\sigma}$ can be written as

$$\sigma_{ij} = (1-\xi)\sigma^f_{ij} + \xi\sigma^e_{ij}, \tag{2.3}$$

where the superscripts ^{f} and ^{e} denote the fluid and the elastic material, respectively; ξ is the local solid volume fraction, changing smoothly from 0 in the fluid phase to 1 in the elastic layer within a few Eulerian grid cells. In particular, the isoline at $\xi = 0.5$ represents the interface. The scalar ξ is transported by the local velocity via an advection equation

$$\partial_t \xi + u_i \partial_i \xi = 0. \tag{2.4}$$

The Cauchy stress tensor $\boldsymbol{\sigma}$ for a Newtonian fluid and an incompressible viscous hyper-elastic material can be written, respectively, as

$$\sigma^f_{ij} = -p\delta_{ij} + \mu^f(\partial_j u_i + \partial_i u_j), \tag{2.5}$$

$$\sigma_{ij}^{e} = -p\delta_{ij} + \mu^{e}(\partial_j u_i + \partial_i u_j) + GB_{ij}, \tag{2.6}$$

where p is the pressure, δ_{ij} the Kronecker delta and μ the dynamic viscosity; $G\boldsymbol{B}$ is the hyper-elastic contribution for a neo-Hookean material, satisfying the incompressible Mooney–Rivlin law, with G the modulus of transverse elasticity and $\boldsymbol{B}$ the left Cauchy–Green deformation tensor. The tensor $\boldsymbol{B}$ is updated by the following transport equation

$$\partial_t B_{ij} + u_k \partial_k B_{ij} = B_{kj}\partial_k u_i + B_{ik}\partial_k u_j, \tag{2.7}$$

where the right-hand side of the equation describes the stretching of the elastic material due to the straining action of the flow.

Following the formulations above and taking into account the IBM force, exerted on the fluid phase by the particles, equation (2.1) can be rewritten in its final non-dimensional form,

$$\partial_t u_i + \partial_j u_i u_j = -\partial_i p_e - \partial_i p + \frac{(1-\xi) + \xi\mu^{e/f}}{Re_b}\partial_j\partial_j u_i + \xi G^{*}\partial_j B_{ij} + f_i, \tag{2.8}$$

where $\partial_i p_e$ is the external uniform pressure gradient that drives the flow with a constant bulk velocity U_b, p is the modified pressure (the total pressure minus p_e), Re_b is the bulk Reynolds number, $\mu^{e/f}$ denotes the dynamic viscosity ratio and G^{*} is the non-dimensional elastic modulus, normalized by ρU_b^2. The additional term, $\boldsymbol{f}$, on the right-hand side of equation (2.8), is the IBM acceleration field, active in the immediate vicinity of a particle surface to enforce the no-slip and no-penetration boundary conditions.

The flow field is resolved numerically on a uniform (cubic), staggered, Cartesian grid while particles are represented by a set of Lagrangian points, uniformly distributed on the surface of each particle. The governing differential equations are discretized using a second-order central finite-difference scheme, except for the advection terms in equations (2.4) and (2.7) where the fifth-order weighted essentially non-oscillatory (WENO) scheme is applied (Sugiyama *et al.* 2011; Rosti & Brandt 2017; Izbassarov *et al.* 2018). An explicit third-order Runge–Kutta scheme (Breugem 2012) is used for the time integration of all terms in equations (2.4), (2.7) and (2.8) without considering the IBM acceleration field $\boldsymbol{f}$, except for the solid hyper-elastic contribution, which is advanced in time with the Crank–Nicolson method (Min, Yoo & Choi 2001). The first prediction velocity obtained after the time integration step is then used to compute the point forces $\boldsymbol{F}_l$ (normalized by $\rho\Delta V_l$, with ΔV_l being the volume of each Lagrangian grid point, equal to the volume of an Eulerian grid cell) at each Lagrangian point on the surface of the particles, based on the difference between the particle surface velocity and the interpolated first prediction velocity at that point. The singular forces $\boldsymbol{F}_l$ are then spread into the IBM acceleration field $\boldsymbol{f}$ using the regularized Dirac delta function δ_d of Roma, Peskin & Berger (1999); $\boldsymbol{f}$ is then added to the first prediction velocity followed by the pressure-correction scheme used in Breugem (2012) to project the velocity field in the divergence-free space. More details and validations of the numerical scheme can be found in Breugem (2012), Ardekani *et al.* (2016), Rosti & Brandt (2017), Izbassarov *et al.* (2018), Rosti, Brandt & Mitra (2018*a*).

Taking into account the inertia of the fictitious fluid phase trapped inside the particle volumes, the motion of the rigid particles is described by the Newton–Euler

Lagrangian equations,

$$\rho_p V_p \frac{\mathrm{d}\boldsymbol{u}_p}{\mathrm{d}t} = -\rho \sum_{l=1}^{N_L} \boldsymbol{F}_l \Delta V_l + \rho \frac{\mathrm{d}}{\mathrm{d}t}\left(\int_{V_p} \boldsymbol{u}\,\mathrm{d}V\right) + (\rho_p - \rho) V_p \boldsymbol{g} + \boldsymbol{F}_c, \tag{2.9}$$

$$\boldsymbol{I}_p \frac{\mathrm{d}\boldsymbol{\Omega}_p}{\mathrm{d}t} = -\rho \sum_{l=1}^{N_L} \boldsymbol{r}_l \times \boldsymbol{F}_l \Delta V_l + \rho \frac{\mathrm{d}}{\mathrm{d}t}\left(\int_{V_p} \boldsymbol{r} \times \boldsymbol{u}\,\mathrm{d}V\right) + \boldsymbol{T}_c, \tag{2.10}$$

with $\boldsymbol{u}_p$ and $\boldsymbol{\Omega}_p$ being the translational and the angular velocity of the particle; ρ_p, V_p and $\boldsymbol{I}_p$ are the particle mass density, volume and moment-of-inertia tensor; and $\boldsymbol{g}$ the gravity vector. The first term on the right-hand side of the equations above describes the IBM force and torque as the summation of all the point forces $\boldsymbol{F}_l$ on the surface of the particle, the second term accounts for the inertia of the fictitious fluid phase trapped inside the particle and $\boldsymbol{F}_c$ and $\boldsymbol{T}_c$ are the force and the torque due to the particle–particle interactions.

When the distance between the particles is smaller than one Eulerian grid cell, the lubrication force is under-predicted by the IBM. To compensate for this inaccuracy and to avoid computationally expensive grid refinements, a lubrication correction model based on the asymptotic analytical expression for the normal lubrication force between spheres (Jeffrey 1982) is used. A soft-sphere collision model with Coulomb friction takes over the interaction when the particles touch. The restitution coefficients used for normal and tangential collisions are 0.97 and 0.1, with the Coulomb friction coefficient set to 0.15. More details about these models can be found in Costa *et al.* (2015), Ardekani *et al.* (2016).

A sub-grid repulsive lubrication-like force $\boldsymbol{F}_r$ (Clift, Grace & Weber 2005; Bolotnov *et al.* 2011; De Vita *et al.* 2019) is employed to model the particle–interface interactions when the distance between a particle and the interface is less than 1.5 Eulerian grids. This sub-grid repulsive force is written as

$$\boldsymbol{F}_r = \frac{1}{2}\mu^f U_b D_p \left(\frac{a_1}{d_w} + \frac{a_2}{d_w^2}\right) \boldsymbol{n}_w, \tag{2.11}$$

with a_1 and a_2 being two coefficients, set to 550 and 55 in this study, $\boldsymbol{n}_w$ is the unit vector normal to the wall and d_w is the distance from the interface; μ^f is the fluid viscosity in this formulation (De Vita *et al.* 2019).

2.2. *Flow geometry*

We perform direct numerical simulations of pressure-driven, particulate turbulent channel flow, bounded by two incompressible hyper-elastic walls at $y = 0$ and $y = 2h$, with h being half of the distance between the two interfaces. A computational domain of size $L_x = 6h$, $L_y = 2(h + h_e)$ and $L_z = 3h$ is considered in the streamwise, wall-normal and spanwise directions, where $h_e = 0.25h$ is the height of the elastic walls in the flat unstressed condition. Two impermeable walls are located at $y = -h_e$ and $y = 2h + h_e$ with no-slip and no-penetration (n.s./n.p.) boundary conditions, while the flow is considered periodic in the two wall-parallel directions. The bulk velocity U_b is fixed to guarantee a constant bulk Reynolds number $Re_b \equiv 2hU_b/\nu_f = 5600$. This corresponds to an average friction Reynolds number of $Re_\tau \equiv u_\tau h/\nu_f \approx 180$ in the case of unladen flow over flat rigid walls (Kim, Moin & Moser 1987) with ν_f and u_τ being the fluid kinematic viscosity and the friction velocity, respectively. The

Case	$Re_b \equiv U_b h/\nu_f$	$G^* \equiv G/(\rho U_b^2)$	h_e/h	$\phi(\%)$	N_p	h/D_p	$Re_\tau \equiv u_\tau h/\nu_f$
$G1$	5600	0.25	0.25	0	0	—	388.4
$G2$	5600	0.5	0.25	0	0	—	281.1
$G3$	5600	1	0.25	0	0	—	197.2
$G4$	5600	2	0.25	0	0	—	184.8
$G1_{10\,\%}$	5600	0.25	0.25	10	5000	9	351.4
$G2_{10\,\%}$	5600	0.5	0.25	10	5000	9	262.8
$G3_{10\,\%}$	5600	1	0.25	10	5000	9	225.1
$G4_{10\,\%}$	5600	2	0.25	10	5000	9	212.7
$G2_{5\,\%}$	5600	0.5	0.25	5	2500	9	273.1
$G2_{20\,\%}$	5600	0.5	0.25	20	10 000	9	231.5
$G1_{FW}$	5600	—	—	0	0	—	280.2
$G4_{NPWL}$	5600	2	0.25	10	5000	9	166.8

TABLE 1. Summary of the simulations performed in this study, all for a bulk Reynolds number $Re_b = 5600$. Here, h_e is the height of the elastic walls in the flat unstressed condition, G^* is the non-dimesionalized modulus of transverse elasticity, ϕ denotes the particle volume fraction and N_p the number of the particles inside the domain with diameter $D_p = h/9$. All simulations are performed on a computational domain of size $6h \times 2(h + h_e) \times 3h$ in the streamwise, wall-normal and spanwise directions, discretized with $1296 \times 540 \times 648$ grid cells. Re_τ is the resulting mean friction Reynolds number, reported here for all the simulated cases.

same viscosity is considered in this study for the elastic layer and the fluid phase ($\nu^f = \nu^e$), as it was shown before that the elasticity modulus G is the key parameter affecting the interface and the flow dynamics (Rosti & Brandt 2017).

Four different moduli of transverse elasticity G are studied here, ranging from an almost rigid interface, $G^* = 2$, to a highly elastic case of $G^* = 0.25$. Particulate cases are simulated at each G^* with a particle volume fraction $\phi = 10\,\%$ and the results are compared to the unladen flow with the same wall elasticity. We consider non-Brownian neutrally buoyant rigid spherical particles with diameter $D_p = h/9$. This corresponds to 5000 particles inside the computational domain at $\phi = 10\,\%$, see Picano *et al.* (2015). The effect of volume fraction is further studied at a moderate wall elasticity of $G^* = 0.5$, by decreasing and increasing the particle volume fraction to $\phi = 5\,\%$ and $20\,\%$.

Two additional numerical experiments are performed to gain a better understanding of the flow: (i) a simulation, denoted $G1_{FW}$ (fixed wall), where an instantaneous configuration of the deformed interface, extracted from the case with the highest wall elasticity, is frozen so as to distinguish the effect on the near-wall turbulence of wall elasticity from the modulation caused by random roughness and (ii) case $G4_{NPWL}$ (no particle-wall layer), where particles are forced to bounce back towards the core region of the channel before approaching the deformable walls; this is achieved by numerical collisions with the two virtual walls located at a distance of $h/10$ from the two undeformed interfaces. A summary to the simulated cases is given in table 1.

The simulations are performed on a uniform Cartesian grid of size $1296 \times 540 \times 648$, corresponding to a resolution of 24 grid points per particle diameter D_p in the particulate cases. The number of Lagrangian points N_L on the surface of each particle is set to $N_L = 1721$. All cases are started from a fully developed turbulent channel flow in the fluid region ($y = 0$ to $2h$) with a perfectly flat interface (initially) and a random distribution of the particles. The statistics are collected for approximately

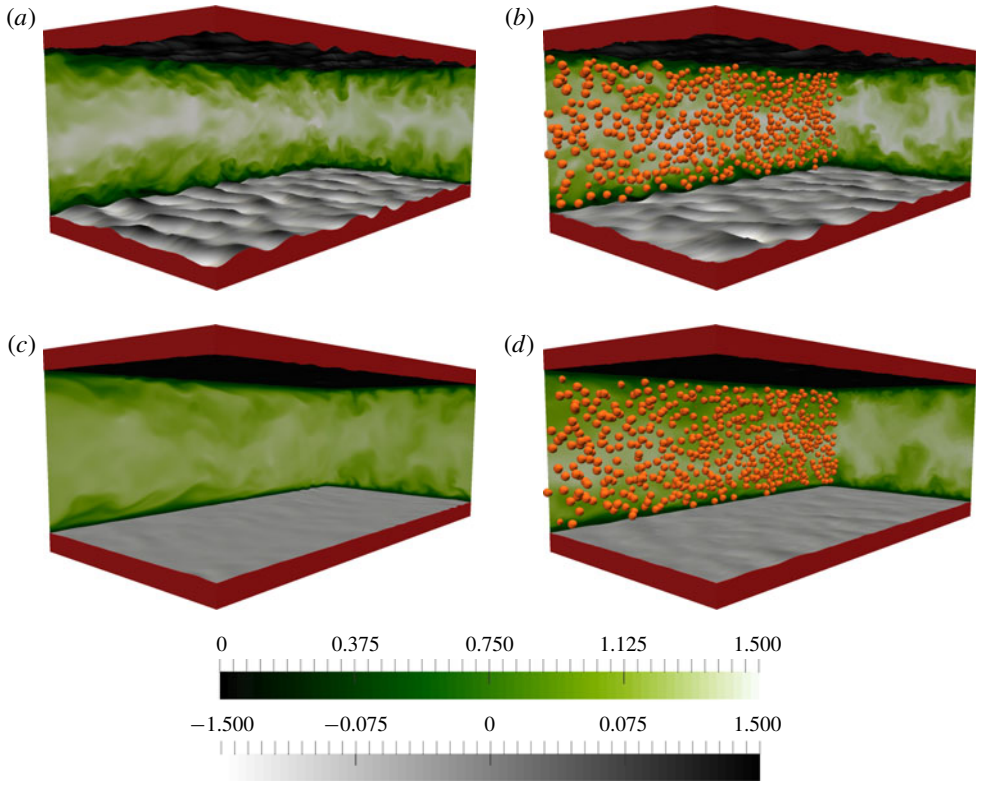

FIGURE 1. (Colour online) Instantaneous snapshots of the streamwise velocity u on x–y and y–z planes for (*a*) $G^* = 0.25$ (case $G1$), (*b*) $G^* = 0.25$ at $\phi = 10\,\%$ (case $G1_{10\,\%}$), (*c*) $G^* = 1$ (case $G3$) and (*d*) $G^* = 1$ at $\phi = 10\,\%$ (case $G3_{10\,\%}$). For clarity, only the particles cutting the selected x–y plane are displayed. The colour scale for the streamwise velocity ranges from 0 (dark green) to $1.5u/U_b$ (white). The elastic walls are represented by the isosurfaces of $\xi = 0.5$, coloured by the wall-normal distance, ranging from $-0.15h$ (white) to $0.15h$ (black).

$600h/U_b$ after the flow has reached a statistical steady state. The pressure gradient, required to maintain the constant bulk velocity U_b, is monitored in time and used as a criterion for deciding a statistically steady state condition. A Courant–Friedrichs–Lewy number of 0.2 is used to guarantee the numerical stability of the method. It should be noted here that the simulations with the most elastic walls ($G^* = 0.25$) are slightly under-resolved due to the considerably smaller viscous length scale for these cases, however the results are reported here to show the trend against the wall elasticity.

3. Results

3.1. *Drag & deformation*

We first display snapshots of the flow and particles in figure 1, where the instantaneous streamwise velocity u is depicted on x–y and y–z planes for the cases with $G^* = 0.25$ and 1 at $\phi = 0$ and 10 %. For clarity, just a fraction of the particles (those cutting the visualized x–y plane) are displayed. Comparing with respect to the single-phase flow at the same wall elasticity (figure 1*a*), particles are observed to decrease the wall

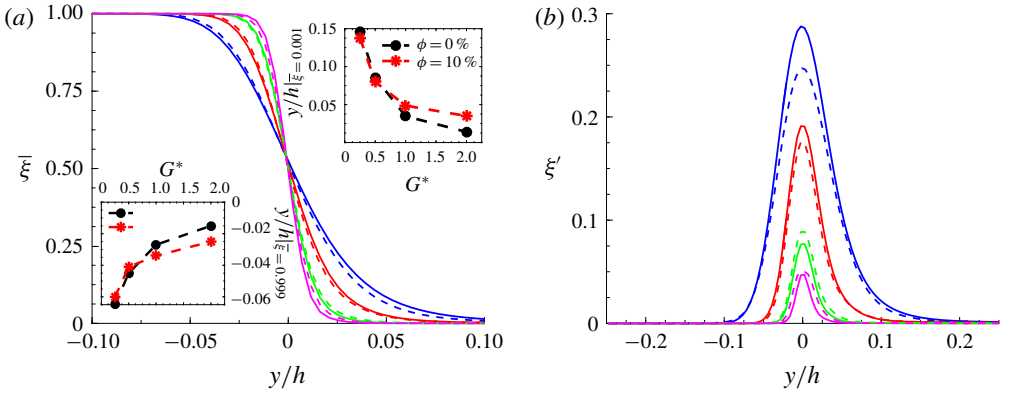

FIGURE 2. (Colour online) VoF function ξ versus the normalized distance from the interface y/h, showing the wall deformation for the different cases under investigation: (a) mean values and (b) root-mean-square (r.m.s.) of the fluctuations in ξ. The blue, red, green and magenta solid lines are used for the cases $G1$ to $G4$, respectively, while the particulate cases $G1_{10\,\%}$ to $G4_{10\,\%}$ are indicated with dashed lines of the same colour. The insets in (a) show the maximum and minimum position of the interface for different wall elasticities.

deformation and turbulence activity in $G1_{10\,\%}$ (figure 1b). However, the opposite effect is observed in $G3_{10\,\%}$ (figure 1c,d), where the wall deformation is slightly increased in the presence of the particles. Also interesting to note is the spanwise coherency of the wall deformation in figure 1(a), which is broken into a less correlated pattern in the particulate case $G1_{10\,\%}$ (see figure 7 for a quantitative comparison).

To provide a quantitative measure of the wall deformation, the mean ($\overline{\xi}$) and root-mean-square (ξ') profiles of the VoF function ξ representing the elastic walls are depicted in figure 2 versus the normalized distance from the interface y/h. The maximum and minimum of the interface position, corresponding to the highest crests and the lowest troughs of the wavy interface, defined by the locations where $\overline{\xi}$ attains the values 0.999 and 0.001, are reported in the insets of figure 2(a) for the different wall elasticities considered.

The results show an expected decrease of wall deformation with increasing G^* for both single-phase and particulate cases. However, the effect of the particles on the wall deformation is non-monotonic: we find a slight decrease with respect to the single-phase flow in the cases with highly elastic walls ($G1_{10\,\%}$ and $G2_{10\,\%}$), and a larger interface deformation for the cases with less wall elasticity in the presence of particles ($G3_{10\,\%}$ and $G4_{10\,\%}$). Although the particles do not significantly change the maximum amplitude of the deformation, the approach of $\overline{\xi}$ to zero and one (insets of figure 2a) is considerably modified: the data reveal the less frequent occurrence of large deformations in the particulate case at low G^* and the opposite behaviour at high G^*. The profiles of ξ', depicted in figure 2(b), The peak value at $y = 0$ indicates the degree of waviness at the interface. Given that $\overline{\xi} = 0.5$ at the $y = 0$ plane, the peak of ξ' is bounded between $\xi' = 0.5$, where all the grid points in the $y = 0$ plane are located inside the fluid region or in the elastic layer, and $\xi' = 0$, where the interface is undeformed everywhere. The results show a decrease of the interface waviness by the presence of the particles in highly elastic walls, while the opposite is evident in the less deformable cases. This behaviour is attributed to the

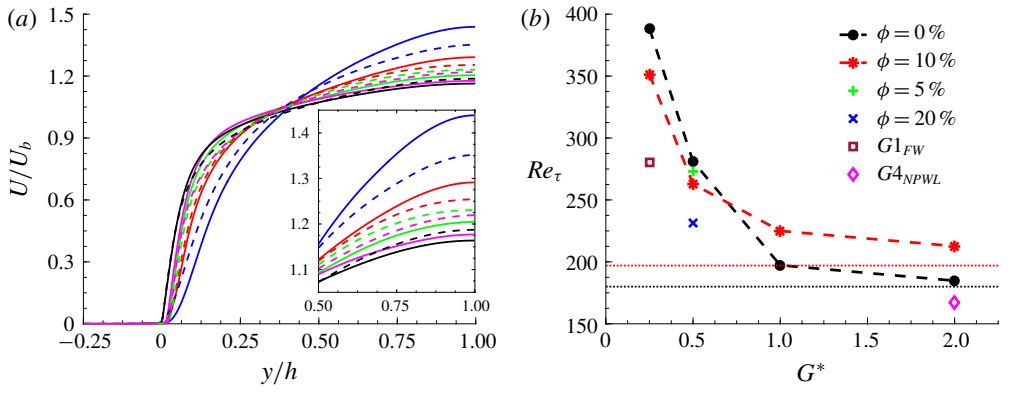

FIGURE 3. (Colour online) (*a*) Mean velocity profiles, normalized by the bulk velocity U_b. The colour scheme is the same as figure 2 with two extra black lines, pertaining to the results for rigid walls (Ardekani *et al.* 2017): a solid line for single-phase flow and a dashed line for particulate flow at $\phi = 10\,\%$. The inset displays the increase of the mean velocity in the core of the channel. (*b*) The friction Reynolds number Re_τ versus the modulus of transverse elasticity G^*. The black and red dashed horizontal lines in (*b*) represent Re_τ for the single-phase and the particulate flow over smooth rigid walls.

particle migration towards the centre of the channels with highly elastic walls and its resulting turbulence attenuation (see the next sections for the details).

The mean velocity profiles, obtained by averaging in the fluid phase, are presented in figure 3(*a*), together with two extra lines, pertaining to the results for rigid walls (Ardekani *et al.* 2017). Note that the mean velocity inside the elastic walls is equal to zero. The results show that the mean velocity increases with the wall elasticity at the channel centreline for both particulate and single-phase cases, whereas it decreases close to the interface. Similarly to the flow over rigid walls (Picano *et al.* 2015; Ardekani *et al.* 2017), particles are observed to increase the core velocity, except for the cases with highly elastic walls ($G1_{10\,\%}$ and $G2_{10\,\%}$), where the core velocity is reduced in their presence. We note here that unlike the single-phase flows over rigid walls, the mean velocity reduction close to the interface should not be interpreted as a sign of drag reduction. In fact, the friction Reynolds number Re_τ, depicted in figure 3(*b*), indicates a significant drag increase with growing wall elasticity. Note that, Re_τ is calculated using the mean pressure gradient needed to keep U_b constant. Therefore, we find drag reduction with respect to the single-phase flow for same wall elasticity only for the particulate cases with highly elastic walls. Results concerning the case $G4_{NPWL}$ with artificially removed particle-wall layer and the cases with different volume fractions, $G2_{5\,\%}$ and $G2_{20\,\%}$, will be discussed in § 3.3 and § 3.4. A comparison is made in appendix A between the results, pertaining to the single-phase flow and the case $G1_{FW}$ to distinguish the main effects of wall elasticity on the near-wall turbulence from the modulation caused by the roughness.

To better understand the overall drag, we perform a momentum budget analysis. In particulate turbulent flows with rigid walls, the particle-induced stress contributes to the mean momentum transfer, in addition to the viscous and Reynolds shear stresses. Here, we extend the formulation proposed by Zhang & Prosperetti (2010), Picano *et al.* (2015) for the momentum balance in particulate flows, by taking the hyper-elastic contribution into account (Rosti & Brandt 2018). The mean momentum balance

in the channel then reads

$$\rho u_\tau^2 \left(1 - \frac{y}{h}\right) = \mu(1-\Phi)\frac{\mathrm{d}U}{\mathrm{d}y} - \rho[\Phi\langle u_p' v_p'\rangle + (1-\Phi)\langle u'v'\rangle] + \langle \xi G B_{xy}\rangle + \Phi\langle \sigma_{xy}^p\rangle, \quad (3.1)$$

where the first term on the right-hand side is the viscous shear stress, denoted τ_V, the second and the third terms indicate the turbulent Reynolds shear stress of the combined phases, τ_T, the fourth term is the contribution of the hyper-elastic wall, τ_E and the fifth term is the particle-induced stress τ_P; σ_{xy}^p in the equation above indicates the stress in the particle phase, normal to the streamwise plane and pointing in the wall-normal direction, Φ is the mean local particle volume fraction as a function of the wall-normal distance and u' and v' are the velocity fluctuations in the streamwise and wall-normal directions with the subscript $_p$ denoting the particle phase. Here, ρ and μ are the density and viscosity, assumed equal in the fluid and the elastic layer. Note that in the absence of particles ($\Phi = 0$) and the elastic layer ($\xi = 0$), this equation reduces to the classic momentum balance for single-phase turbulent channel flow (Pope 2000).

The wall-normal profiles of each term in the momentum transfer, normalized by ρu_τ^2, are displayed in figure 4(*a–d*) for the cases $G1$, $G1_{10\,\%}$, $G4$ and $G4_{10\,\%}$. Note that the particle stress τ_P is computed by subtracting the three other stresses from the total stress. Close to the interface, the contribution from the viscous stress τ_V is reduced significantly with increasing wall elasticity, as the mean velocity is shown to decrease in this region (figure 3*a*). The hyper-elastic stress, τ_E, instead, takes over the momentum transfer, growing linearly within the elastic layer, where all other terms in equation (3.1) tend to zero. Note that, this line can be extrapolated to calculate the exact wall drag at $y = 0$, obtaining a drag which is consistent with the ones reported above based on the mean pressure gradient. Far from the interface region, the Reynolds stress, τ_T, plays the main role in momentum transfer. The relative importance of the particle stress τ_P is observed to increase with the wall elasticity, while the peak close to the interface disappears.

Integrating equation (3.1) from 0 to h leads to the contribution of each stress to the total τ_w, which can be written as

$$\tau_w = \frac{2}{h}[\Sigma\tau_V + \Sigma\tau_T + \Sigma\tau_E + \Sigma\tau_P]. \quad (3.2)$$

Each contribution, multiplied by $2/h$ and normalized with the wall shear stress of the single-phase flow over rigid walls (τ_{RW}), is reported in figure 4(*e*,*f*) for the single-phase and the particulate cases with different wall elasticities; RW and $RW_{10\,\%}$ are obtained from the simulations with rigid walls presented in Ardekani *et al.* (2017). Overall, we observe that the increase in drag with wall deformability can be attributed to an increase of the turbulence activity, as also discussed in Rosti & Brandt (2017). In other words, the turbulence activity increases with respect to the reference RW for all cases. The contribution of the viscous shear stress to the total drag is in general reduced with increasing wall elasticity, whereas the particle stress $\Sigma\tau_P$ monotonically increases with decreasing G^*. This can be explained by the rigid particles opposing any deformation, while experiencing stronger forces on their surfaces due to the growing turbulence activity with decreasing G^*. We also note a non-monotonic variation of $\Sigma\tau_T$ and $\Sigma\tau_E$ in the particle-laden cases when comparing the results with the single-phase flows of the same wall elasticity: turbulence attenuation for highly elastic walls, while increasing the turbulence activity in the cases of less deformable walls.

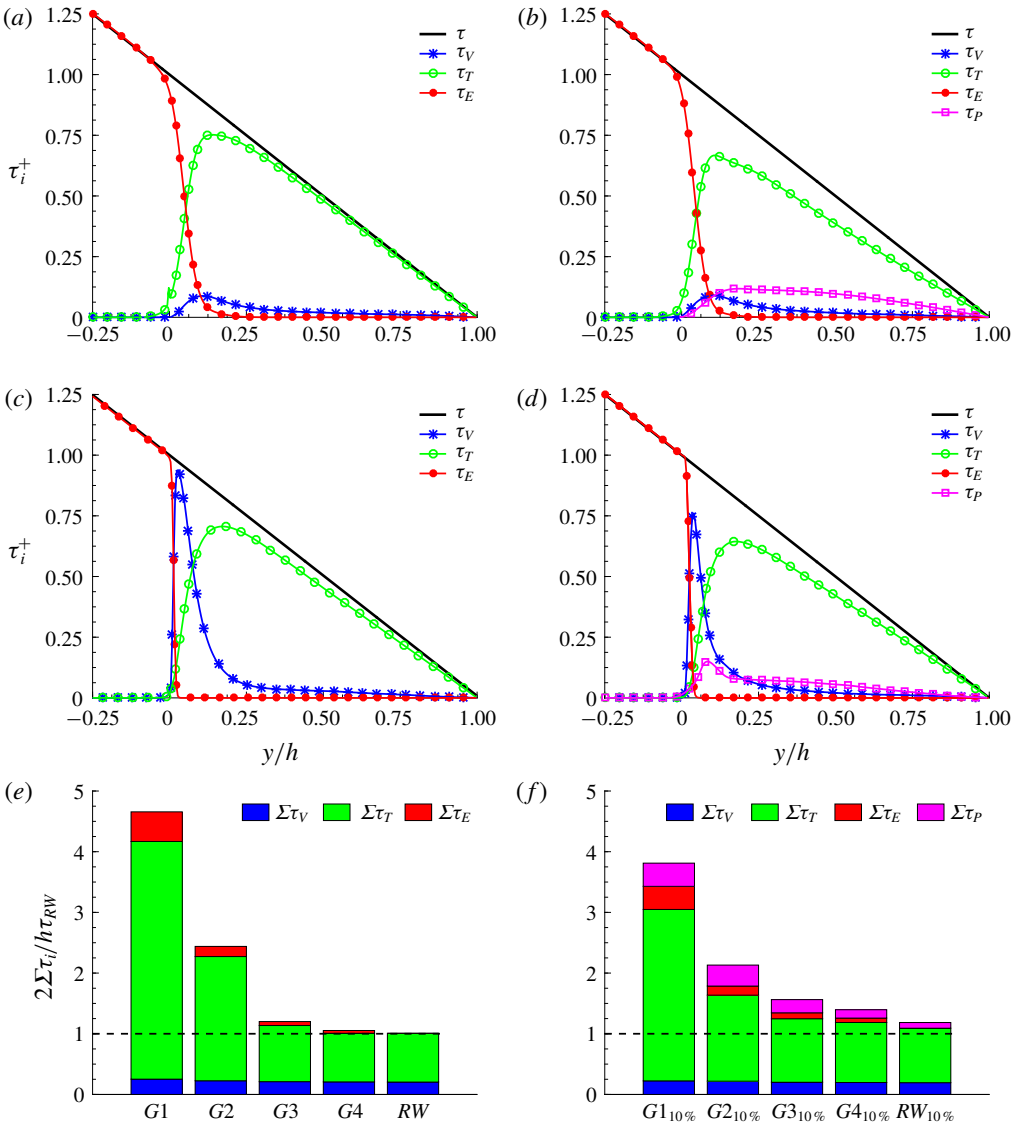

FIGURE 4. (Colour online) Momentum budget, normalized with ρu_τ^2, for (*a*) $G1$, (*b*) $G1_{10\%}$, (*c*) $G4$ and (*d*) $G4_{10\%}$. Here, τ is the total stress, τ_V the viscous shear stress, τ_T the turbulent Reynolds shear stress of the combined phases, τ_E the hyper-elastic contribution and τ_P the particle induced stress. Panels (*e*) and (*f*) show the total contribution of each stress to the drag, normalized by the wall shear stress of the single-phase flow with rigid walls, τ_{RW} (the dashed line in the figure). *RW* and $RW_{10\%}$ are the cases with rigid walls taken by Ardekani *et al.* (2017).

3.2. *Turbulence modulation*

In this section we take a closer look at the turbulence modulation caused by the simultaneous presence of the particles and deformable walls. We first examine the root-mean-square velocity fluctuations and the Reynolds shear stress profiles, depicted in figure 5. The velocity fluctuations are strongly affected by the elastic layer,

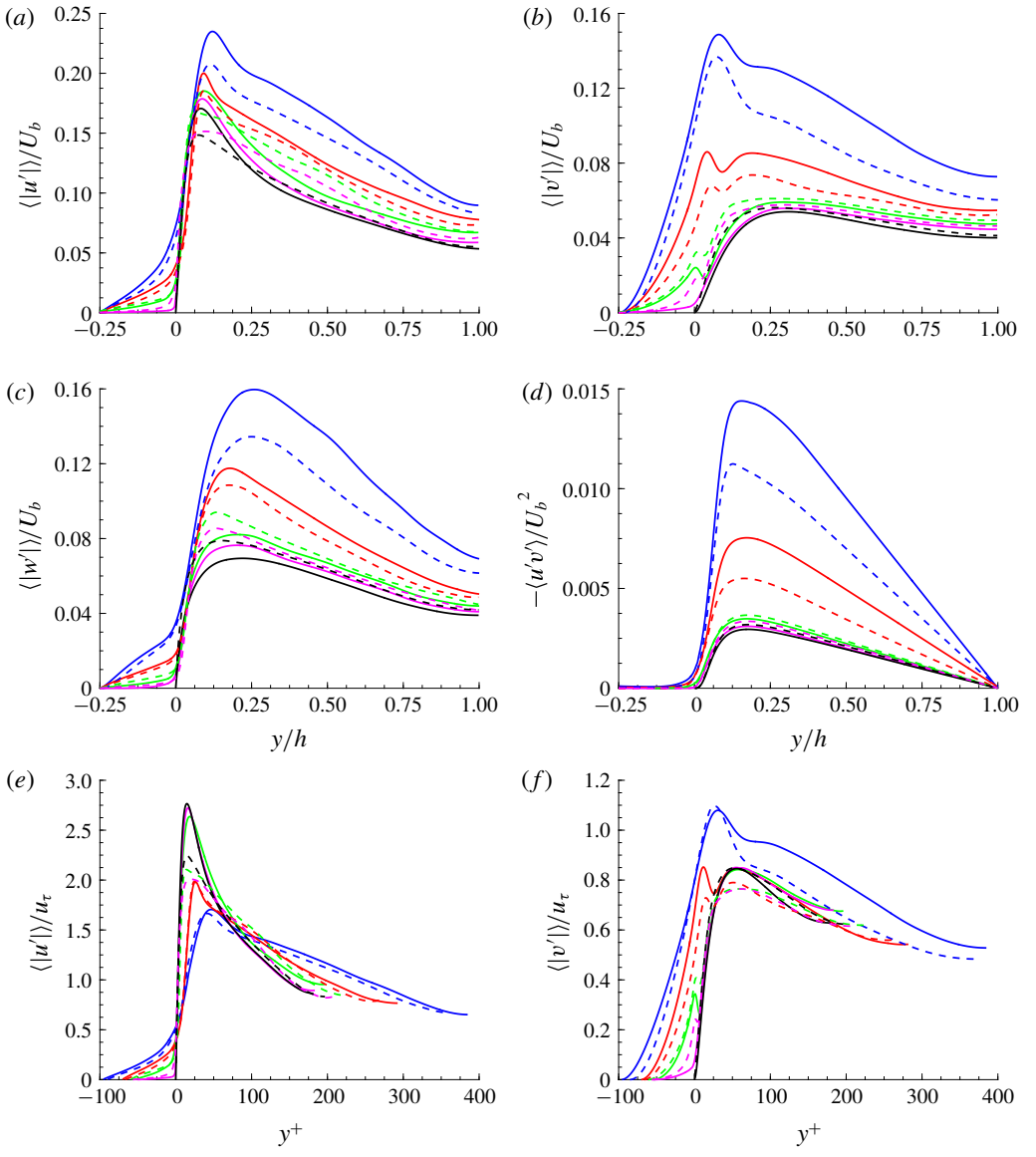

FIGURE 5. (Colour online) Root-mean-square velocity fluctuations and Reynolds shear stress: (*a*) streamwise $\langle|u'|\rangle$; (*b*) wall normal $\langle|v'|\rangle$; (*c*) spanwise $\langle|w'|\rangle$ and (*d*) Reynolds shear stress. Panels (*e*) and (*f*) show $\langle|u'|\rangle$ and $\langle|v'|\rangle$, scaled in internal units. The colour scheme is the same as in figures 2 and 3(*a*).

lingering inside as the wall elasticity increases. The wall-normal velocity fluctuation v' is the most affected by the wall elasticity, owing to the weakening of the wall blocking and wall-induced viscous effects (Perot & Moin 1995*a*,*b*). The same effect is also observed in turbulent boundary-layer flows over rough (Krogstadt & Antonia 1999) and porous walls (Rosti, Brandt & Pinelli 2018*b*). In addition, we note that $\langle|v'|\rangle$ attains a secondary peak in the vicinity of the interface, associated with the oscillatory interface motion. As the wall elasticity increases, this secondary peak

moves farther from the interface, becomes stronger than the classical turbulent peak and the fluctuations are larger at the interface. In addition, we note that the peak of the streamwise velocity fluctuations, u', increases with increasing wall elasticity considerably less than in the other two directions, which we attribute to the quenching of the near-wall streaky structures close to the deformable interface (Breugem *et al.* 2006; Rosti & Brandt 2017; Rosti *et al.* 2018*b*). This behaviour is particularly evident in figure 5(*e*,*f*), where the profiles of $\langle|u'|\rangle$ and $\langle|v'|\rangle$ are depicted in internal units.

The magnitude of the velocity fluctuations increases in the presence of particles for low wall deformabilities while it decreases for high elasticity, except for the peaks of $\langle|u'|\rangle$ which are always reduced with respect to their single-phase counterparts. Despite the strong velocity fluctuations also inside the highly elastic walls, the Reynolds shear stress (see figure 5*d*) is zero within these layers, indicating a decorrelation of u' and v'. The Reynolds shear stress increases in the particulate cases, except in the presence of highly elastic walls, as observed for the r.m.s. velocities, where a significant attenuation is instead observed (also shown in figure 4*f*).

Next, we take a closer look at the turbulent flow near the deformable walls, see figure 6 where we report instantaneous snapshots of the streamwise velocity fluctuations, u', in the wall-parallel plane at $y/h = 0.1$. The so-called high- and low-speed streaks, characteristic of wall-bounded turbulence, can be directly recognized near the less elastic walls. As the wall elasticity increases (from bottom to top), these streamwise streaky structures appear as less elongated and more fragmented, broken into smaller pieces by the interface motion. Further increasing the wall elasticity results in the formation of relatively large structures, now correlated in the spanwise direction (*a*), similar to those observed by Rosti & Brandt (2017). These spanwise structures have been observed before in the turbulent flow over porous walls (Breugem *et al.* 2006; Rosti *et al.* 2015, 2018*b*), rough surfaces (Raupach, Antonia & Rajagopalan 1991; Jiménez *et al.* 2001) and plant canopies (Finnigan 2000). Breugem *et al.* (2006) relates these elongated structures to a Kelvin–Helmholtz-type instability that is triggered by the inflection point of the mean velocity profiles (Rayleigh's criterion, see Drazin & Reid 2004), creating spanwise vortices or rollers. Snapshots of u' in the flow laden with particles are shown in figure 6(*b*,*d*,*f*,*h*). Particles can be observed to break both the streamwise and the spanwise structures into less elongated and more fragmented patches.

To gain a better understanding of the turbulence structures and in order to quantify the observations in figure 6, we compute the two-point spatial correlation of the streamwise and the wall-normal velocity fluctuations as a function of the spanwise and streamwise spacing, respectively as

$$R^{z}_{uu}(y,\,\Delta z) = \frac{\langle u'(x,\,y,\,z,\,t)u'(x,\,y,\,z+\Delta z,\,t)\rangle}{u'^{2}}, \tag{3.3}$$

$$R^{x}_{vv}(y,\,\Delta x) = \frac{\langle v'(x,\,y,\,z,\,t)v'(x+\Delta x,\,y,\,z,\,t)\rangle}{v'^{2}}. \tag{3.4}$$

Line and colour contours of $R^{z}_{uu}(y,\,\Delta z)$ and $R^{x}_{vv}(y,\,\Delta x)$ are presented in figure 7(*a*,*b*) for the different cases under investigation. It is known that in a single-phase turbulent flow the spanwise correlation of the streamwise velocity fluctuations exhibits a negative local minimum in the near-wall region at around $\Delta z^{+} \approx 50$–60 (Pope 2000), which indicates half of the spacing between two neighbouring streaks. A similar spacing is obtained in figure 7(*a*) for the cases with less elastic walls *G*3 and *G*4 (top right), as these display a local minimum at $\Delta Z^{+} \approx 55$ and $\Delta Z^{+} \approx 58$, respectively.

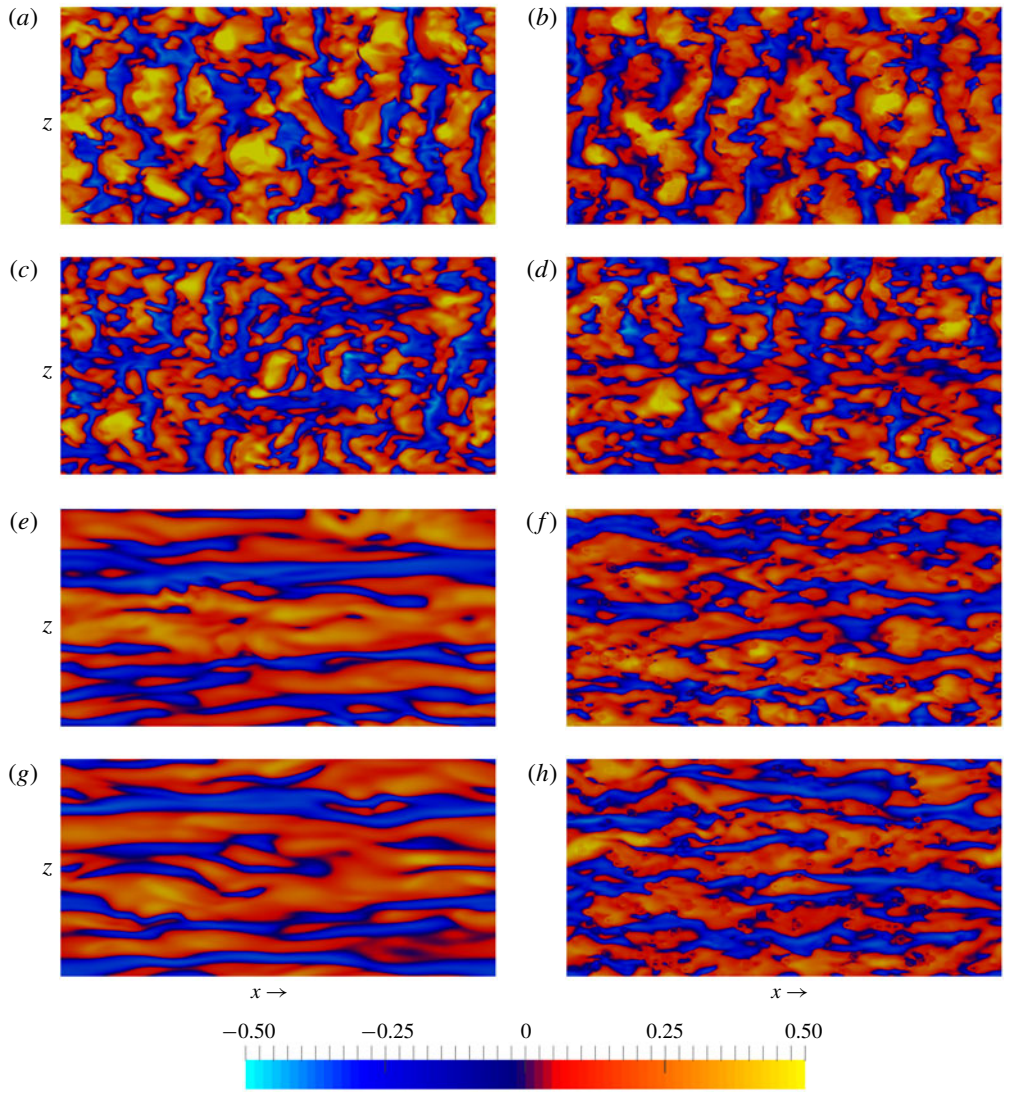

FIGURE 6. (Colour online) Instantaneous contours of the streamwise velocity fluctuations u' in the wall-parallel plane $x-z$ at $y/h=0.1$. The colour scale goes from $-0.5U_b$ (blue) to $0.5U_b$ (yellow). (*a*,*c*,*e*,*g*) indicates the single-phase flow cases ($G1$ to $G4$) and (*b*,*d*,*f*,*h*), the particulate ones ($G1_{10\,\%}$ to $G4_{10\,\%}$), with G^* increasing from (*a*–*h*).

The figure shows clearly the disruption of the high- and low-speed streaks, when increasing the wall elasticity, and how they shift away from the interface region. The absence of high- and low-speed streaks, close to the highly elastic walls, can be attributed to (i) a strong reduction of the mean shear (see figure 3*a*), an important ingredient in the streaks formation mechanism (Lee, Kim & Moin 1990; Brandt 2014) and (ii) strong wall-normal velocity fluctuations preventing the development of elongated structures. A region of positive values of R^z_{uu} can be observed instead, at $y/h \approx 0.1$ and 0.07 for the highly elastic cases, $G1$ and $G2$: this indicates the

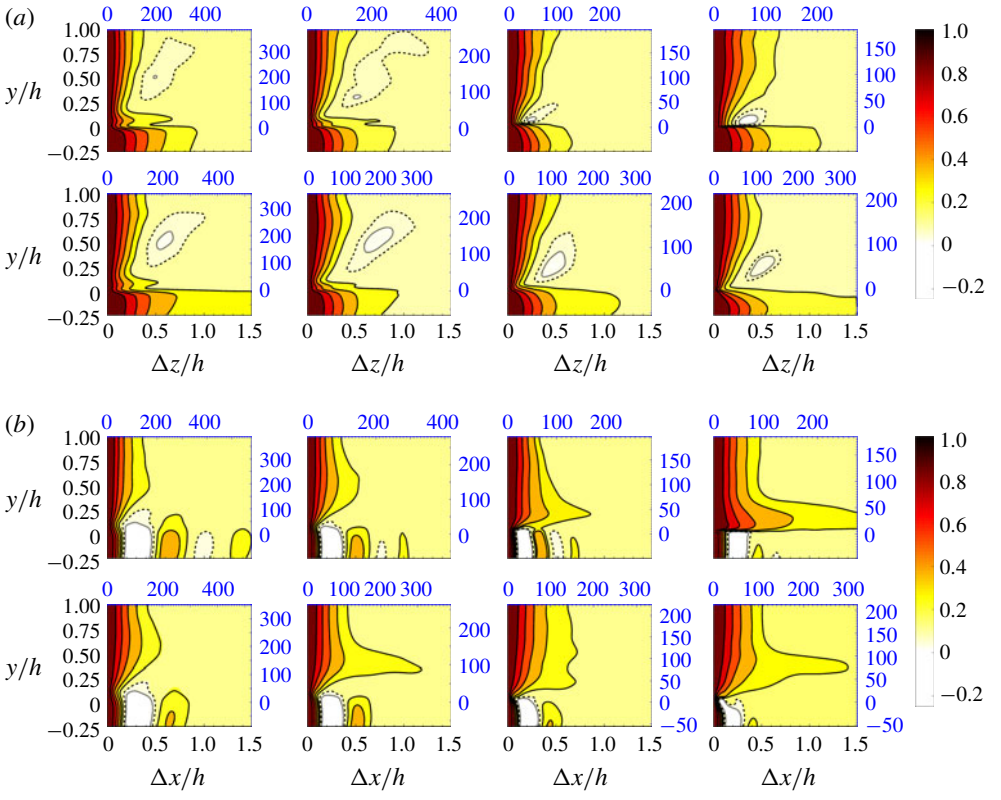

FIGURE 7. (Colour online) Line and colour contours of the one-dimensional autocorrelation of (*a*) the streamwise velocity fluctuations as a function of the spanwise spacing ($R^z_{uu}(y, \Delta z)$) and (*b*) the wall-normal velocity fluctuations as a function of the streamwise spacing for different y/h ($R^x_{vv}(y, \Delta x)$). The solid lines correspond to positive values, ranging from 0 to 0.8 with a step of 0.2 between two neighbouring lines, whereas dashed and dotted lines indicate the isolines at −0.1 and −0.2, respectively. Results, pertaining to the single-phase flow (cases $G1$ to $G4$), are shown in the first row of each panel, while the autocorrelations for the particulate cases (cases $G1_{10\%}$ to $G4_{10\%}$) are depicted in the second row. G^* increases from left to right. Internal units are indicated on the top and on the right side of each panel.

emergence of structures elongated in the spanwise direction (as expected from the visualizations in figure 6) with an approximate length of 0.7–0.8h.

The correlation R^z_{uu} pertaining to the particulate cases is given in the second row of figure 7(*a*). The addition of particles shortens the spanwise length of the structures in the cases $G1_{10\%}$ and $G2_{10\%}$; the wall elasticity disrupts and displaces the high- and low-speed streaks towards the channel centre. The disruption of the near-wall streaks has been reported before for turbulent channel flows of finite-size spherical particles (Picano *et al.* 2015; Costa *et al.* 2018; Wang, Abbas & Climent 2018; Ardekani & Brandt 2019).

Next, we show the autocorrelations of the wall-normal velocity fluctuations along the streamwise direction $R^x_{vv}(y, \Delta x)$, see figure 7(*b*). The results clearly reveal that the long quasi-streamwise vortices, associated with the presence of streaks, vanish when increasing the wall elasticity and are replaced by roller-type vortices, elongated

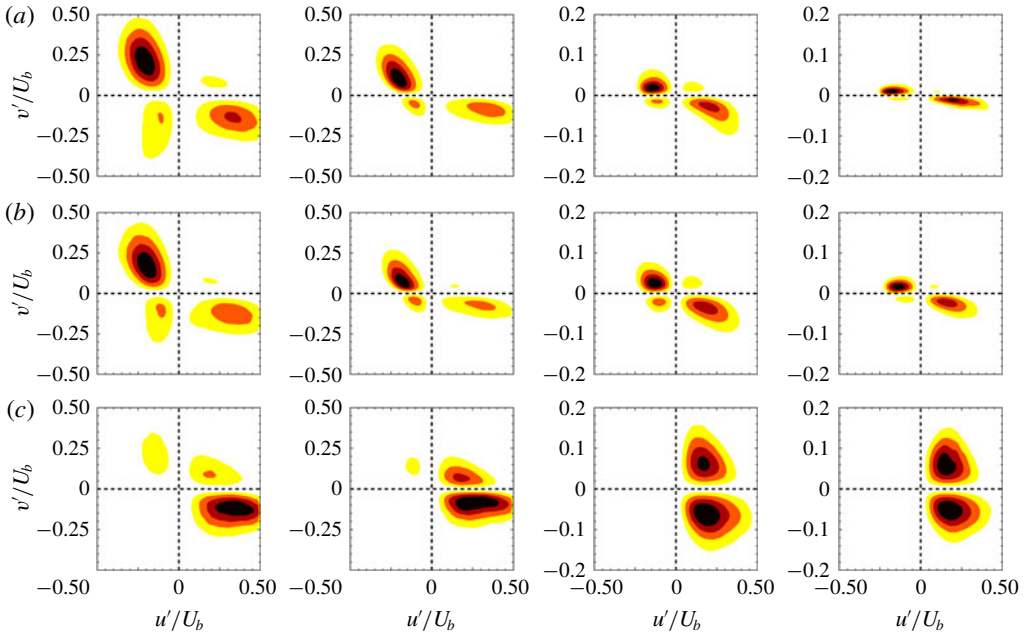

FIGURE 8. (Colour online) Contours of the weighted Reynolds shear stress at $y/h = 0.05$, given by multiplying the absolute value of the Reynolds shear stress by the joint probability density of its occurrence in the u'–v' plane for: (*a*) the single-phase flow cases $G1$ to $G4$, (*b*) the particulate cases $G1_{10\,\%}$ to $G4_{10\,\%}$ and (*c*) spherical shells 5 % larger than the particles in $G1_{10\,\%}$ to $G4_{10\,\%}$. G^* increases from left to right and the colours go from yellow to black (maximum).

in the spanwise direction. The active range of these vortical structures grows with the wall elasticity, reaching a size of approximately 140^+ in the most elastic case $G1$. In the particle-laden flows, the height of these vortices reduces in the highly elastic cases, whereas the quasi-streamwise vortices characteristic of the less deformable cases become shorter and more irregular. Breaking the large spanwise vortices near highly elastic walls results in less wall deformation and thus, an overall attenuation of the turbulent activity (see also figure 1*b*); however, it should be also noted that breaking the quasi-streamwise vortices does not necessarily decrease the turbulent activity. Indeed, it has been shown before that spherical particles with the same size and volume fraction as considered here induce an increase of the turbulent activity near rigid walls (Picano *et al.* 2015; Ardekani *et al.* 2017), similarly to what observed in this study for the less elastic cases (see figure 5*d*).

So far we have presented a picture of the turbulence coherent structures near elastic walls, including the presence of finite-size particles; however, the way these structures contribute to the enhancement or attenuation of the Reynolds shear stress is yet to be understood. To this purpose, we compute the weighted Reynolds shear stress, obtained by multiplying the absolute value of Reynolds shear stress with the joint probability density of its occurrence in the u'–v' plane (Zhou *et al.* 1999). This analysis indicates the turbulent events that contribute the most to the Reynolds shear stress, dividing them into the four quadrants of the u'–v' plane, denoted Q_1 to Q_4. In particular, Q_2 (ejections: $u' < 0$, $v' > 0$) and Q_4 (sweeps: $u' > 0$, $v' < 0$) events result in turbulence production, while Q_1 and Q_3 are responsible for damping.

Contours of the weighted Reynolds shear stress are depicted in figure 8 for a wall-parallel plane slightly above the elastic wall $y/h = 0.05$; $y/h = 0.05$ approximately matches the particle radius and is chosen to indicate the effect of the particles close to the wall on the near-wall turbulence. Panel (*a*) shows the results for the single-phase cases with elasticity decreasing from left to right. The major contribution to the turbulence production near the highly elastic walls comes from ejection events with significantly large values of v' and small negative u'; the contribution of sweeps comes from the events with an opposite combination, i.e. small negative v' and a relatively large positive u'. This observation reveals the mechanism by which the spanwise vortices, forming close to the highly elastic walls, contribute to the turbulence production: these vortices bring down the high momentum flow towards the elastic wall with a weak wall-normal velocity due to the decreased wall-blocking effect of the elastic layer, thus deforming the interface. The interface then releases this elastic energy by pushing the flow with a strong wall-normal velocity towards the centre of the channel, contributing to the turbulence production and regeneration of new spanwise vortical structures. The low magnitude of u' in the ejection events is believed to be due to the blocking effect from the upstream deformed interface. This is consistent with the asymmetric shape of the deformed wall (steeper slope for wall retraction), previously shown in figure 1(*a*). As the wall elasticity decreases, the distribution of the strong ejection events over the u'–v' plane appears to become less elongated in the vertical direction (v' axis), while stretching along the u' axis. The relative contribution of sweep events increases when lowering the wall elasticity, although with smaller magnitudes of $u'v'$. The distribution for the least elastic case (*b*) is similar to what found in turbulent flows in the vicinity of rigid walls (Kim *et al.* 1987), where the sweep events are slightly more powerful than the ejections.

The results pertaining to the particulate cases are depicted in figure 8(*b*). The shapes of the distribution are similar to the ones of the single-phase flow cases, except for an increase ($G3_{10\,\%}$ and $G4_{10\,\%}$) or a reduction ($G1_{10\,\%}$ and $G2_{10\,\%}$) in the magnitude of v'. To gain a better understanding of the particles role, we repeat the same analysis in figure 8(*c*), now sampling only the fluid inside a spherical shell which is 5 % larger than the particles (particles cutting the wall-normal plane $y/h = 0.05$). For the cases with highly elastic walls, the particles approach the interface region and are trapped inside strong sweep events with a relatively large streamwise velocity. The asymmetry in the magnitude of the wall-normal fluctuations (larger magnitudes for positive v') causes the particles to move away from the wall considerably faster than when approaching it. Therefore, it is more likely to sample particles which are slowly approaching the wall, surrounded by Q_4 events. It should be noted here that the particle concentration is low in the vicinity of highly elastic walls as we will discuss later in § 3.3 and thus, the strong sweep events around the particles do not contribute significantly to the turbulent production. Indeed, particles reduce the active range of the large spanwise vortices, causing smaller wall deformation and in turn a turbulence attenuation. In addition to sweeps, stronger Q_1 events appear in the flow surrounding the particles when the wall elasticity decreases. This is due to particles with large streamwise velocity bouncing back from the less deformable walls. Even though Q_1 events damp the turbulence activity, the increase in the wall-normal velocity fluctuations and also stronger sweeps close to the wall result in an overall enhancement of the turbulent activity. The same conclusion can be drawn from figure 9, where the Reynolds shear stress is conditionally averaged and depicted for the second (Q_2) and the fourth (Q_4) quadrants of the u'–v' plane against y/h. Interestingly, both ejection and sweep events are damped in the presence of the

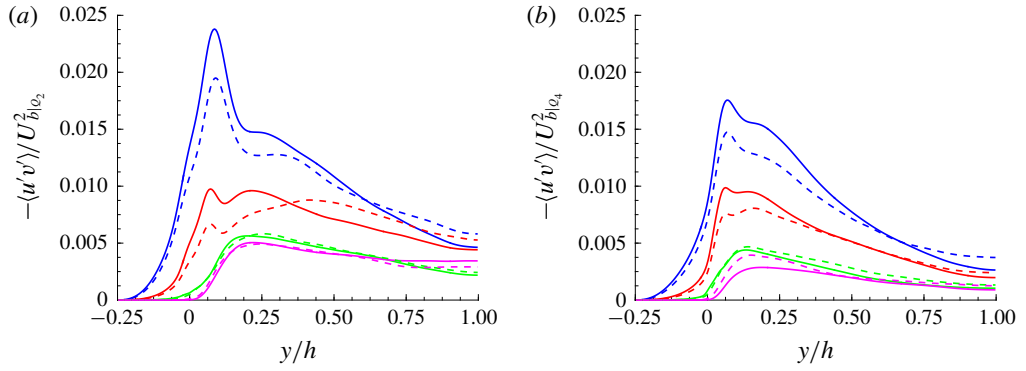

FIGURE 9. (Colour online) Reynolds shear stress, conditionally averaged for (*a*) the second (Q_2) and (*b*) the fourth (Q_4) quadrant of u'–v' plane.

particles for the highly elastic walls; while for the less elastic cases, turbulence is enhanced through sweep events and ejections are almost unchanged with respect to the single-phase cases.

3.3. *Particle dynamics*

The mean local volume fraction Φ is depicted in figure 10(*a*). Spherical particles in the turbulent flow with rigid walls (case $RW_{10\,\%}$) display a local maximum at a distance slightly larger than one particle radius from the wall. Picano *et al.* (2015) attributed this local maximum to the formation of a particle layer at the wall due to the wall–particle interactions that stabilize the particle position. Costa *et al.* (2016) further explained that the presence of this particle layer always results in drag increase with respect to the single-phase flow. Interestingly, the local maximum for Φ is observed to reduce and move farther away from the wall when increasing the wall elasticity. The migration of the particles from the interface region can be explained by the presence of the strong ejection events with large v' in the flow in the case of highly elastic walls (see figure 8). Indeed, the strong asymmetry in the magnitude of the wall-normal velocity fluctuations, which favours positive v', pushes the inertial particles towards the channel centre. However, as the wall elasticity decreases, a more symmetric distribution of v' allows the particles to form a layer close to the interface, similarly to the rigid wall cases. This particle-wall layer contributes to the turbulent production by increasing the cross-flow velocity fluctuations, as shown in the previous subsection.

To study the particle dynamics, we display in figure 10(*b*) the ratio between the turbulent kinetic energy of the fluid and that of the particle phase, $K'_f/K'_p = \langle u'^2 + v'^2 + w'^2\rangle/\langle u_p'^2 + v_p'^2 + w_p'^2\rangle$. For the particle statistics presented in this figure the rigid body motion of the particles is taken into account. The local velocity of the particle phase is computed at each point by $\boldsymbol{u}_p + \boldsymbol{\Omega}_p \times (\boldsymbol{x} - \boldsymbol{x}_c)$, with $\boldsymbol{x}$ and $\boldsymbol{x}_c$ denoting an arbitrary point inside the particle and the particle centre, respectively. Particle velocities are observed to fluctuate less than the fluid at the same wall-normal distance, except for a tiny region close to the wall ($y/h \lessapprox 0.05$), where the ratio is below 1 for all the cases. The high particle fluctuation level in this region suggests that this is the cause of the near-wall enhancement of the fluid velocity fluctuations, observed in the cases with less elastic walls. The ratio between the two energies increases with the wall

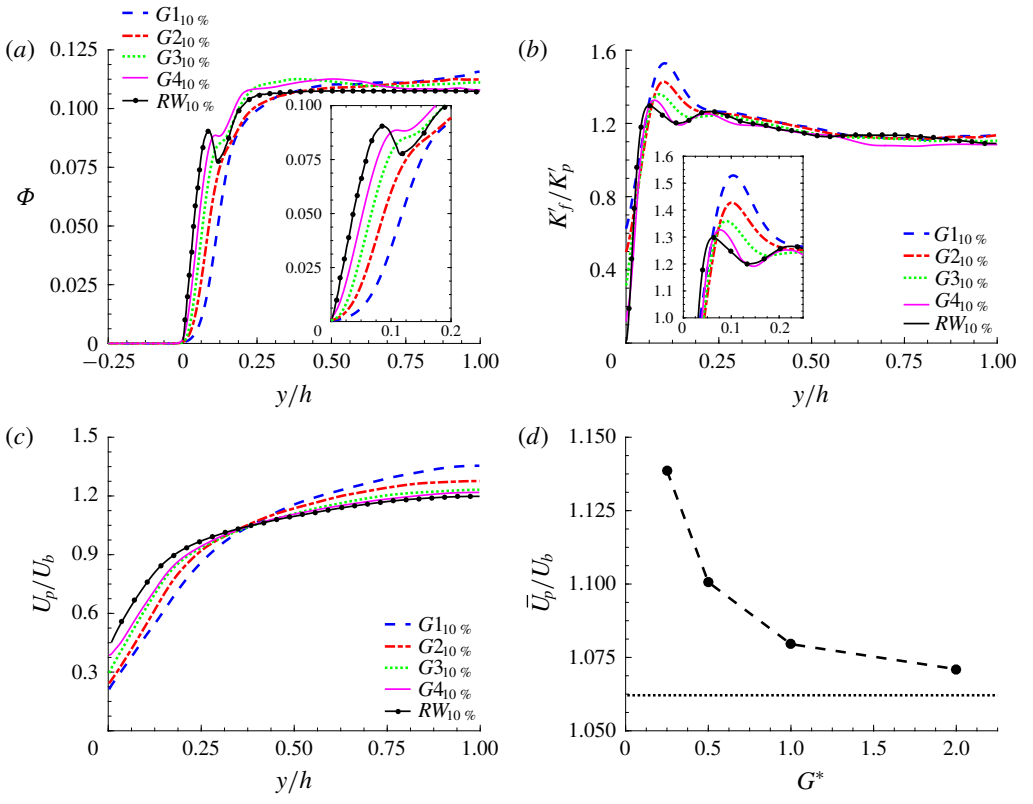

FIGURE 10. (Colour online) Profiles of particle-phase averaged data versus y/h: (*a*) mean local volume fraction, (*b*) the ratio between the turbulent kinetic energy of the fluid and of the particle phase and (*c*) mean particle velocity profiles, normalized by the bulk velocity U_b. $RW_{10\,\%}$ refers to the case with rigid walls from the study of Ardekani *et al.* (2017). (*d*) Overall average particle velocity versus the modulus of transverse elasticity G^*. The average of the particle velocity for $RW_{10\,\%}$ is indicated with a dotted line.

elasticity at $y = 0$, reaching 0.6 in the most elastic case, when fewer particles can be found in this region. Particle–wall/particle collisions are observed to play an important role in increasing the fluctuations near the wall. Indeed, the particles in this region have a mean velocity larger than the surrounding fluid, due to their size and the fact that they can have a relative tangential motion at the wall. Therefore, any collision between the particles can result in strong velocity fluctuations. Figure 10(*c*) depicts the mean particle velocity profiles, normalized by the bulk velocity U_b. Comparing the profiles with the mean velocity in figure 3(*a*) reveals that the particle and fluid phase have the same mean velocity throughout the channel, except for a small layer close to the wall with the width of approximately one particle diameter D, where particles experience a larger mean velocity. The slip velocity at $y = 0$ is observed to increase as the wall elasticity decreases.

The overall average particle velocity is displayed in figure 10(*d*) versus the modulus of transverse elasticity G^*. It can be observed in this figure that increasing the wall elasticity results in a faster transport of the solid phase as the averaged velocity increases from approximately $1.06U_b$ in the case of rigid walls (shown with a dotted horizontal line) to 1.14 in the flow over the most elastic walls. This increase in the

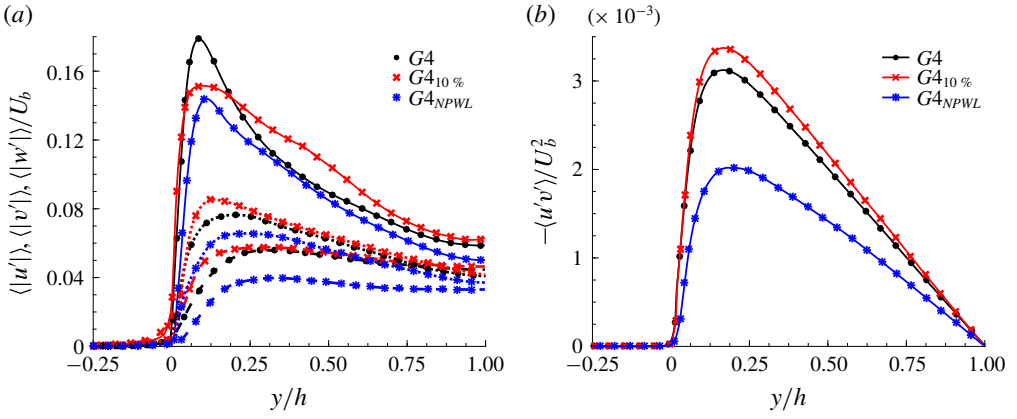

FIGURE 11. (Colour online) (*a*) Root-mean-square velocity fluctuations u', v' and w' in the streamwise, ——, wall-normal, - - - and spanwise, . . . , directions and (*b*) Reynolds shear stress, scaled in outer units for the cases $G4$, $G4_{10\,\%}$ and $G4_{NPWL}$.

averaged velocity is due to the migration of the particles away from the interface region.

To show the importance of the particle-wall layer in the enhancement of the velocity fluctuations in this region, we perform a numerical experiment where we artificially remove this layer. In this simulation, denoted $G4_{NPWL}$ (no particle-wall layer), particles bounce back towards the core region of the channel before approaching the elastic walls, colliding with two virtual walls located at a distance $h/10$ from the two real interfaces ($y/h = 0.1$). The elasticity of the wall is set to $G^* = 2$, i.e. the less deformable elastic wall previously considered, the case where the effect of the particle-wall layer is more pronounced. The velocity fluctuations and the Reynolds shear stress pertaining to this additional case are compared with the results for $G4$ and $G4_{10\,\%}$ in figure 11. The increase in the cross-flow fluctuations previously observed for the case $G4_{10\,\%}$ disappears when removing the particle-wall layer ($G4_{NPWL}$), and as a consequence, a strong turbulence attenuation is obtained (see figure 11*b*), with v' the most reduced fluctuation component. With particles not contributing to the turbulent production in the near-wall region, the attenuation of the turbulence activity can be associated with the increased effective viscosity of the suspension (Picano *et al.* 2015; Ardekani *et al.* 2017). The effective viscosity of a rigid particle suspension is always higher than that of the single-phase flow, which cause a reduction in the turbulent activity; however, this effect is usually compensated by the formation of a particle-wall layer and its contribution to the turbulence production, thus resulting in an overall enhancement of the turbulent activity ($G4$). Hence, a strong turbulence attenuation and thus drag reduction ($Re_\tau \approx 167$) even with respect to the single-phase flow over rigid walls ($Re_\tau \approx 180$) can be obtained by removing the particle-wall layer (see figure 3*b*).

3.4. *Effect of the particle volume fraction*

Picano *et al.* (2015) investigated dense suspensions of spherical particles in a turbulent channel flow with rigid walls up to a volume fraction equal to 20 %. Their study revealed that the overall drag increase is mainly due to the enhancement of the turbulence activity up to $\phi = 10\,\%$ and to the particle-induced stress at higher

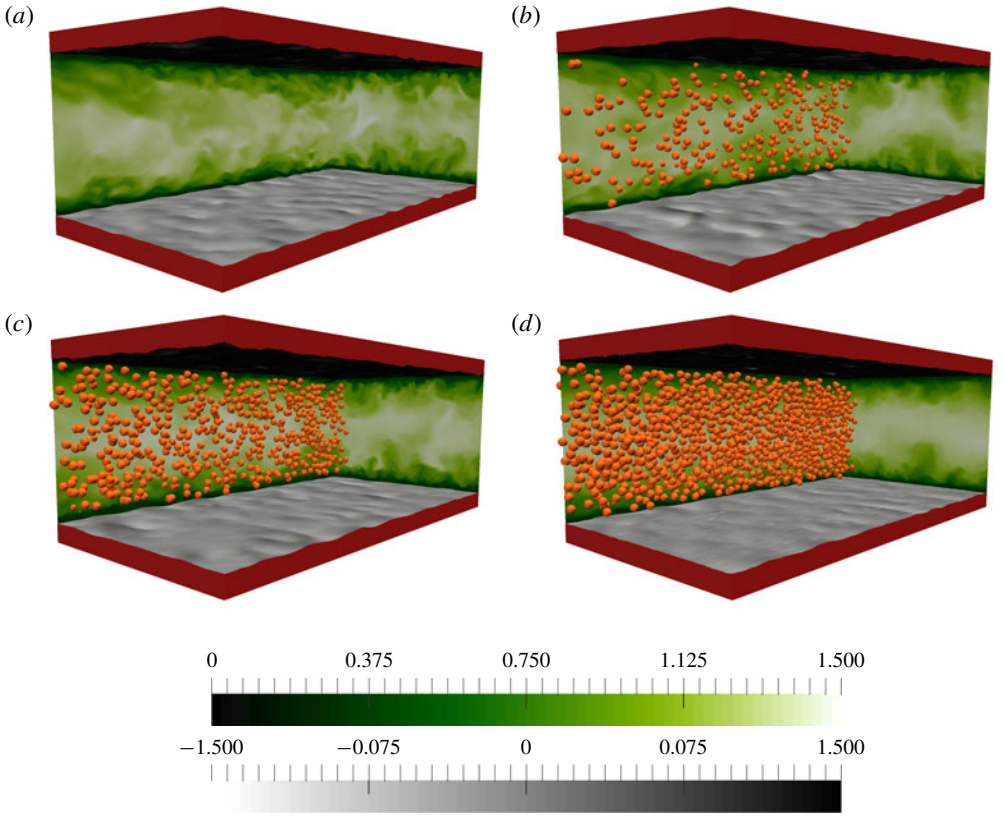

FIGURE 12. (Colour online) Instantaneous snapshots of the streamwise velocity u on the x–y and y–z planes for walls with elastic modulus $G^* = 0.5$ and different volume fractions (*a*) $\phi = 0\,\%$ (case $G2$), (*b*) $\phi = 5\,\%$ (case $G2_{5\,\%}$), (*c*) $\phi = 10\,\%$ (case $G2_{10\,\%}$) and (*d*) $\phi = 20\,\%$ (case $G2_{20\,\%}$). For clarity, only the particles lying within the selected x–y plane are displayed. The colour scale for the streamwise velocity ranges from 0 (dark green) to $1.5u/U_b$ (white). The elastic walls are represented by the isosurface $\xi = 0.5$, coloured by the wall-normal distance, ranging from $-0.15h$ (white) to $0.15h$ (black).

concentrations ($\phi = 20\,\%$), where the turbulence is instead attenuated. In this section we investigate the effect of the particle volume fraction in a channel with elastic walls. The case $G2$, with elasticity $G^* = 0.5$, is simulated with two additional volume fractions, $\phi = 5\,\%$ and $20\,\%$, so to compare the change in drag with respect to the cases with rigid walls.

Snapshots of the flow and particles are displayed in figure 12, where the instantaneous streamwise velocity u is depicted on x–y and y–z planes for the cases with $G^* = 0.5$ and $\phi = 0$, $5\,\%$, $10\,\%$ and $20\,\%$. For clarity, just a fraction of the particles (those lying within the visualized x–y plane) are displayed. The wall deformation and the turbulent activity appear to decrease when increasing the particle volume fraction, especially in the case with $\phi = 20\,\%$. Note also the absence of a particle-wall layer close to the interface, even at highest volume fraction considered here, $\phi = 20\,\%$.

The root-mean-square velocity fluctuations $\langle|u'|\rangle$, $\langle|v'|\rangle$ and $\langle|w'|\rangle$ are depicted in figure 13(*a*), versus the wall-normal distance y/h. The results show a progressive

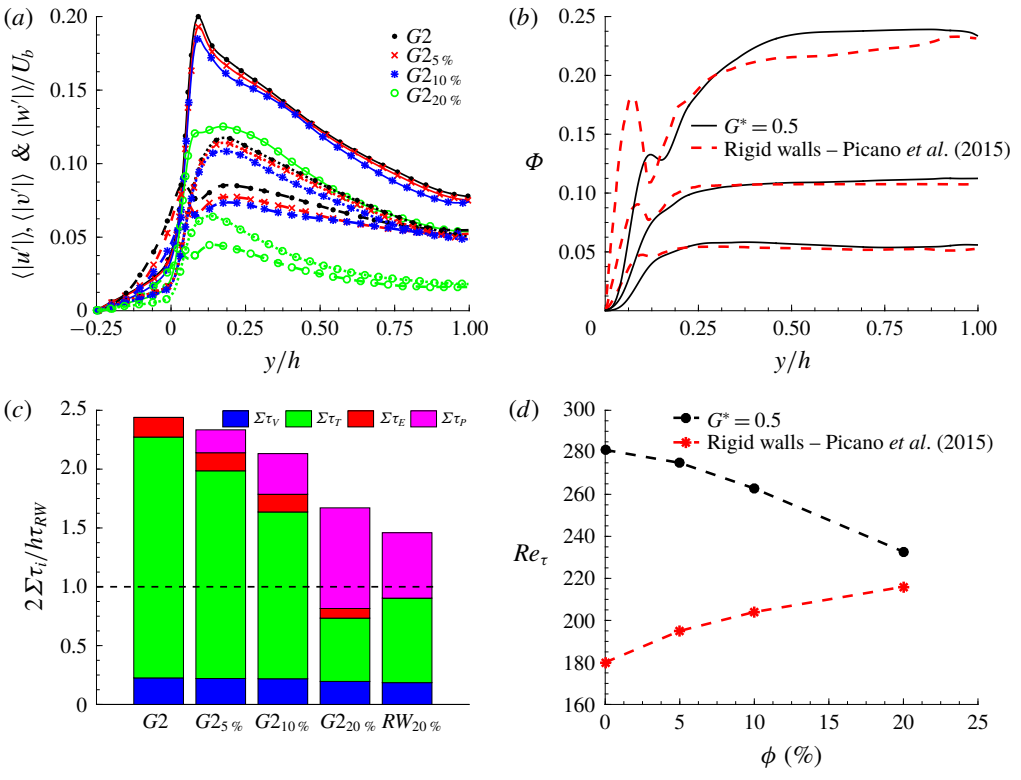

FIGURE 13. (Colour online) (*a*) Root-mean-square velocity fluctuations u', v' and w' in the streamwise, ——, wall-normal, - - -, and spanwise, . . . , directions. (*b*) Mean local volume fraction profiles against the results for rigid walls (Picano *et al.* 2015). (*c*) The total contribution of each stress to the drag at the interface, normalized by the drag of the single-phase flow with rigid walls, τ_{RW} (the dashed line with $Re_\tau = 180$). The case $RW_{20\,\%}$ (rigid walls at $\phi = 20\,\%$) is extracted from the reported data in Picano *et al.* (2015). (*d*) The friction Reynolds number Re_τ, versus the volume fraction ϕ.

reduction in the velocity fluctuations with increasing solid volume fraction. The decrease with respect to $G2$ is moderate for $G2_{5\,\%}$ and $G2_{10\,\%}$, while for a volume fraction of 20 % a significant attenuation of all the velocity fluctuations is evident, especially in the core of the channel where the turbulent flow is almost relaminarized (see also figure 12*d*). Differently from the results with rigid walls (Picano *et al.* 2015), the particles are observed here to attenuate the turbulence activity for all the volume fractions, with a reduction larger than that with rigid walls for the case at $\phi = 20\,\%$. We explain this by examining the mean local volume fraction profiles in figure 13(*b*), where data for rigid walls are also displayed (Picano *et al.* 2015). The particle-wall layer disappears for $\phi \leqslant 10\,\%$ and the near-wall peak is significantly reduced and displaced farther away from the wall ($y/h \approx 0.1$) also for the case $G2_{20\,\%}$. The particle migration away from the interface region causes a stronger attenuation of turbulence than in the presence of rigid walls at $\phi = 20\,\%$.

Following the analysis in equation (3.2), the contribution of each shear stress (viscous, τ_V, Reynolds, τ_T, hyper-elastic, τ_E and particle-induced τ_P), normalized by the drag of the single-phase flow over rigid walls (τ_{RW}), is reported in figure 13(*c*) for different volume fractions at $G^* = 0.5$. The case $RW_{20\,\%}$ denotes the flow at $\phi = 20\,\%$

over rigid walls from Picano *et al.* (2015). In spite of a reduced turbulent activity over an elastic wall, case $G2_{20\,\%}$ in comparison to $RW_{20\,\%}$, the particle stress τ_P more than compensates for the decrease of Reynolds shear stress, resulting in an overall higher drag for the flow over the elastic wall. The friction Reynolds number, Re_τ, is finally compared with the results for rigid walls in figure 13(*d*), where the effect of wall elasticity is observed to reduce significantly when the volume fraction of the particles is increased.

4. Final remarks

We have reported results from direct numerical simulations of single-phase and particulate turbulent channel flows, bounded by two incompressible hyper-elastic walls at bulk Reynolds number 5600 ($Re_\tau \approx [180–380]$). Four different wall elasticities are studied, ranging from an almost rigid to a highly elastic wall. Both single-phase and particulate cases are simulated at each wall elasticity, considering a 10 % volume fraction of finite-size neutrally buoyant rigid spherical particles with a diameter of $D = h/9$ with h the half-channel width.

Our data show a significant drag increase and an enhancement of the turbulent activity with growing wall elasticity for both the single-phase and particle-laden flows. Upon addition of particles, drag reduction and a turbulent attenuation are documented for the flows over highly elastic walls; the opposite is observed for the flow over less elastic walls in which case the drag increases in the presence of the particles.

The strong asymmetry in the magnitude of the wall-normal velocity fluctuations (favouring positive v') is found to push the particles towards the channel centre. However, as the wall elasticity decreases, a more symmetric distribution of v' allows the particles to form a layer close to the interface, similar to the suspension flow over rigid walls. The particle layer close to the wall is shown to contribute to increasing the wall-normal velocity fluctuations, while in the absence of this layer, smaller wall deformation and in turn turbulence attenuation is observed. We further address the importance of the particle-wall layer in turbulence production by performing a numerical experiment where we prevent the formation of this layer for the case with the least elastic walls. In this simulation the particles bounce back towards the core of the channel by colliding with two virtual walls located at a distance $h/10$ from the two real interfaces. The results of this simulation show a strong turbulence attenuation and thus drag reduction ($Re_\tau \approx 167$), even with respect to the single-phase flow over rigid walls ($Re_\tau \approx 180$).

The effect of the volume fraction is further studied at a moderate wall elasticity, by increasing the particle volume fraction up to 20 %. Migration of the particles from the interface region is found to be the cause of an increased turbulence attenuation, when comparing to the flow with same solid volume fraction over rigid walls. However, the particle-induced stress compensates for the decrease of the Reynolds shear stress, resulting in an overall drag increase in the case of elastic walls. The effect of the wall-elasticity on the drag is significantly reduced when the volume fraction of the particles increases.

We finally perform an extra simulation to distinguish the effect of wall elasticity on the near-wall turbulence from the modulation caused by a rough wall (see appendix A). In this simulation, an instantaneous configuration of the deformed interface, obtained in the single-phase case with the highest wall elasticity, is frozen in time. For the flow over this rough wall, the drag is strongly reduced, mostly due to the lower turbulence activity than in the flow over elastic walls. The strong and dominant ejection events, observed in the near-wall turbulence of highly elastic walls, are indeed significantly

reduced near the rough walls. Therefore, we expect that migration of the spherical particles towards the channel centre would be reduced in the case of rough surfaces; this would however require a detailed analysis, left for future studies.

Acknowledgements

This work was supported by the European Research Council Grant no. ERC-2013-CoG-616186, TRITOS. The authors acknowledge computer time provided by SNIC (Swedish National Infrastructure for Computing) and the support from the COST Action MP1305: Flowing matter.

Appendix A. Roughness & elasticity

The single-phase turbulent flow over highly elastic walls shows similarities to what has been reported in the literature for turbulent flows over porous walls (Breugem *et al.* 2006; Rosti *et al.* 2015; Samanta *et al.* 2015; Rosti *et al.* 2018*b*), rough surfaces (Raupach *et al.* 1991; Jiménez *et al.* 2001) and plant canopies (Finnigan 2000). In this section, we wish to distinguish the main effects of wall elasticity on the near-wall turbulence from the modulation caused by the roughness. For this purpose, an additional simulation is performed where an instantaneous configuration of the deformed interface, obtained in the case with the largest wall elasticity ($G1$), is chosen and frozen in time ($G^* \to \infty$). A volume penalization IBM (Kajishima *et al.* 2001; Breugem, Van Dijk & Delfos 2014; Ardekani *et al.* 2018) is employed to impose the no-slip/no-penetration boundary conditions on the surfaces, with the local solid fraction at each grid cell extracted from the instantaneous field ξ in the simulation with deformable walls.

We start by comparing the mean velocity of the single-phase elastic cases with the results obtained for $G1_{FW}$. The mean velocity profiles, scaled in inner units, are depicted in figure 14(*a*), versus $(y+d)^+$. Here, d is a shift of the origin (zero plane) (Jackson 1981; Breugem *et al.* 2006; Suga *et al.* 2010; Rosti & Brandt 2017), following the modified log law

$$U^+ = \frac{1}{k+\Delta k}\log\,(y+d)^+ + B - \Delta U^+. \tag{A 1}$$

Here, $k+\Delta k$ and B are the modified von Kármán and the additive constants ($k=0.4$ and $B=5.5$) and ΔU^+ is the velocity shift; d is calculated similarly to Breugem *et al.* (2006), Rosti & Brandt (2017) by iterating between several values until a region of constant $(y+d)^+\mathrm{d}U^+/\mathrm{d}y^+ = 1/(k+\Delta k)$ is obtained. The mean flow profiles show a significant reduction in the length of the logarithmic layer with increasing wall elasticity, which is not observed for $G1_{FW}$. The values of the fitting parameters, reported in table 2, indicate a downward shift of the inertial range and an increase of its slope with increasing wall elasticities. The mean flow profile for $G1_{FW}$ shows a more pronounced downward shift than the change in slope of the logarithmic layer. Rosti & Brandt (2017) found a linear relation between the wall-normal velocity fluctuations at $y=0$, Δk and the velocity shift ΔU^+,

$$\Delta U^+ \approx \frac{\langle|v'|\rangle(0)}{\Delta k}, \tag{A 2}$$

thus modifying the correlation proposed by Orlandi & Leonardi (2008) for turbulent channel flows over rough walls. This linear correlation is shown in figure 14(*b*) for the

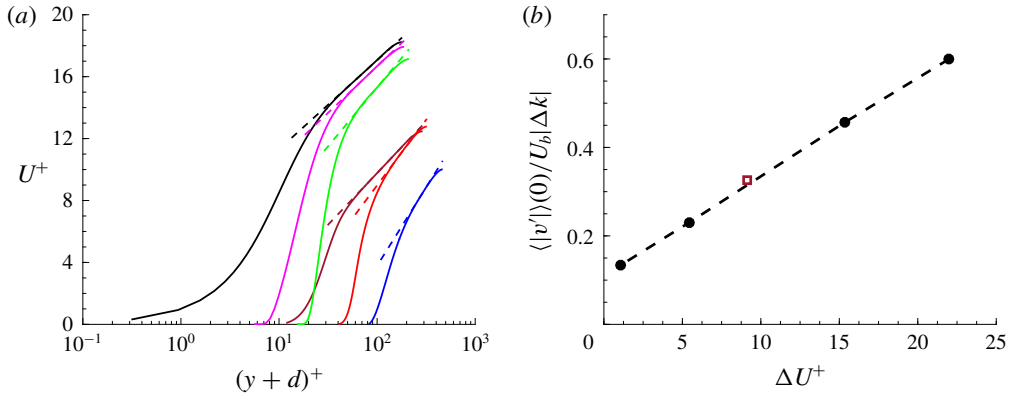

FIGURE 14. (Colour online) (*a*) Mean velocity profiles U^+, scaled in inner units, versus $(y+d)^+$, where d is a shift of the origin. The blue, red, green and magenta solid lines are used for the cases $G1$ to $G4$, respectively, while the profile for $G1_{FW}$ is indicated with a brown solid line. (*b*) Root mean square of the wall-normal velocity fluctuation at $y=0$, divided by $|\Delta k|U_b$, versus the velocity shift ΔU^+. The data for $G1_{FW}$ indicated with a brown square.

Case	d/h	$k+\Delta k$	ΔU^+	$\langle\|v'\|\rangle(0)/U_b$
$G1$	0.211	0.23	22.01	0.108
$G2$	0.143	0.27	15.37	0.064
$G3$	0.075	0.31	5.42	0.023
$G4$	0.028	0.38	1.05	0.004
$G1_{FW}$	0.041	0.35	9.12	0.021

TABLE 2. Summary of the log-law fitting parameters with d the origin shift, $k+\Delta k$ the modified von Kármán constant and ΔU^+ the shift of the mean velocity profile in inner scales. Here, $v'(0)$ denotes the wall-normal velocity fluctuation at $y=0$.

single-phase cases, and interestingly the correlation is also valid for the rough case, depicted with a brown square in this figure. This indicates that the scaling can also be used for rough walls in addition to the elastic walls and the permeable walls, shown to match the correlation in the work of Rosti & Brandt (2017).

The contribution of the different stresses to the global momentum transfer for cases $G1$ and $G1_{FW}$ is reported in figure 15(*a*). Note that τ_E does not indicate the elastic stress for the fixed wall, $G1_{FW}$, but the shear stress from the solid roughness elements acting in the streamwise direction. This is computed with the difference between the total drag (calculated by the imposed pressure gradient) and the sum of the viscous and Reynolds shear stresses inside the channel and is significantly smaller than the contribution of the elastic stress in $G1$. The total drag is reduced from $4.65\tau_{RW}$ to $2.42\tau_{RW}$ in $G1_{FW}$, mostly due to the lower turbulent activity in the flow over the rough walls.

To better understand the cause of this reduction, we display contours of the weighted Reynolds shear stress for the case $G1_{FW}$ at $y/h=0.05$ in figure 15(*b*) (as previously done in figure 8). Interestingly, the strong and dominant ejection events, previously observed for highly elastic walls, are nearly absent close to the rough

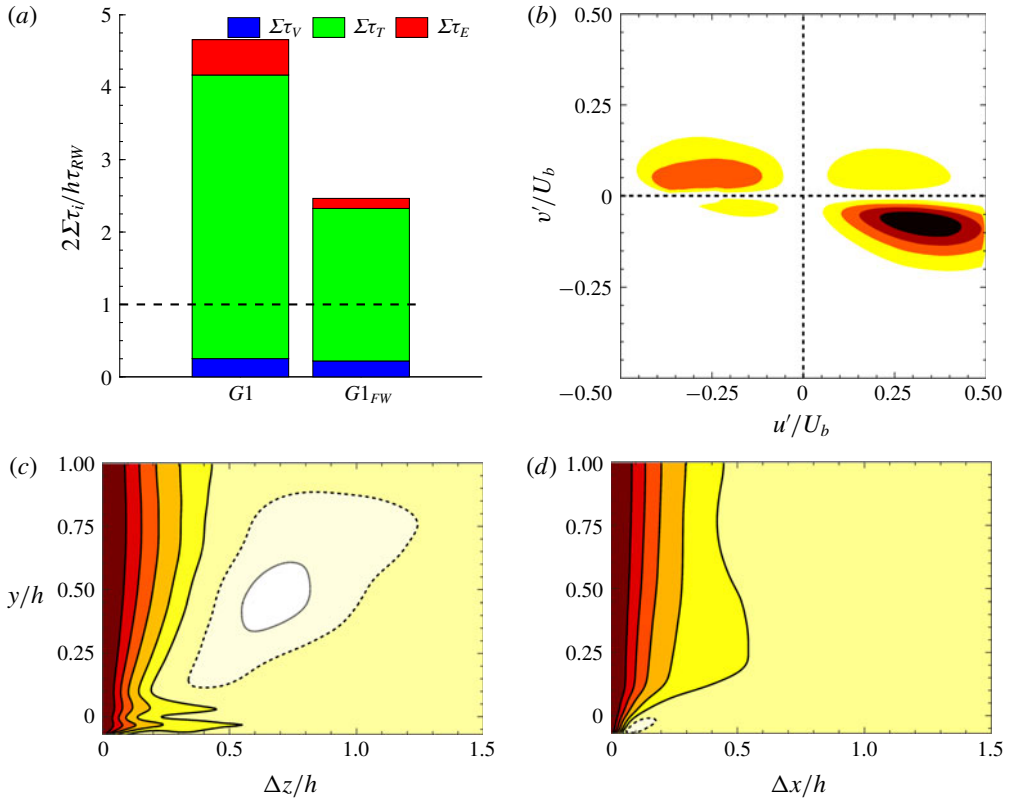

FIGURE 15. (Colour online) (*a*) The contribution of each stress to the total drag, normalized by the drag of the single-phase flow with rigid walls, τ_{RW} (the dashed line with $Re_\tau = 180$). (*b*) Contours of the weighted Reynolds shear stress for $G1_{FW}$ at $y/h = 0.05$, given by multiplying the absolute value of the Reynolds shear stress with the joint probability density of its occurrence in the u'–v' plane. (*c*) One-dimensional autocorrelation of u' as a function of the spanwise spacing ($R^z_{uu}(y, \Delta z)$) and (*d*) one-dimensional autocorrelation of v' as a function of the streamwise spacing for different y/h ($R^x_{vv}(y, \Delta x)$). The colour scheme in (*c*) and (*d*) is the same reported for figure 7.

walls. This further proves that these energetic events are indeed associated with the elastic potential energy of the deformable walls. Sweep events can be observed to be the dominant contribution to the turbulent production near the rough walls, similarly to turbulent flows over permeable walls (Breugem *et al.* 2006; Suga *et al.* 2010) or plant canopies (Zhu, Van Hout & Katz 2007). Finally, line and colour contours of $R^z_{uu}(y, \Delta z)$ and $R^x_{vv}(y, \Delta x)$ are presented in figure 15(*c*,*d*) for the flow over the rigid rough wall. The high- and low-speed streaks are observed to move upwards, with a larger spacing between them. Moreover, the spanwise vortices, previously observed near highly elastic walls, are absent in this case of rough walls. Note that, the two correlated regions (just below and above $y = 0$) in the contours of R^z_{uu} are a consequence of the geometry of the rough surface, which has the spanwise deformations typical of the flow over highly elastic wall, case *G*1.

REFERENCES

ANTONIA, R. A. & KROGSTAD, P.-Å. 2001 Turbulence structure in boundary layers over different types of surface roughness. *Fluid Dyn. Res.* **28** (2), 139.

ARDEKANI, M. N., AL ASMAR, L., PICANO, F. & BRANDT, L. 2018 Numerical study of heat transfer in laminar and turbulent pipe flow with finite-size spherical particles. *Intl J. Heat Fluid Flow* **71**, 189–199.

ARDEKANI, M. N. & BRANDT, L. 2019 Turbulence modulation in channel flow of finite-size spheroidal particles. *J. Fluid Mech.* **859**, 887–901.

ARDEKANI, M. N., COSTA, P., BREUGEM, W. P. & BRANDT, L. 2016 Numerical study of the sedimentation of spheroidal particles. *Intl J. Multiphase Flow* **87**, 16–34.

ARDEKANI, M. N., COSTA, P., BREUGEM, W. P., PICANO, F. & BRANDT, L. 2017 Drag reduction in turbulent channel flow laden with finite-size oblate spheroids. *J. Fluid Mech.* **816**, 43–70.

BEAVERS, G. S., SPARROW, E. M. & MAGNUSON, R. A. 1970 Experiments on coupled parallel flows in a channel and a bounding porous medium. *Trans. ASME J. Basic Engng* **92** (4), 843–848.

BELCHER, S. E., JERRAM, N. & HUNT, J. C. R. 2003 Adjustment of a turbulent boundary layer to a canopy of roughness elements. *J. Fluid Mech.* **488**, 369–398.

BOLOTNOV, I. A., JANSEN, K. E., DREW, D. A., OBERAI, A. A., LAHEY, R. T. JR & PODOWSKI, M. Z. 2011 Detached direct numerical simulations of turbulent two-phase bubbly channel flow. *Intl J. Multiphase Flow* **37** (6), 647–659.

BONET, J. & WOOD, R. D. 1997 *Nonlinear Continuum Mechanics for Finite Element Analysis*. Cambridge university press.

BRANDT, L. 2014 The lift-up effect: the linear mechanism behind transition and turbulence in shear flows. *Eur. J. Mech. (B/Fluids)* **47**, 80–96.

BREUGEM, W-P. 2012 A second-order accurate immersed boundary method for fully resolved simulations of particle-laden flows. *J. Comput. Phys.* **231** (13), 4469–4498.

BREUGEM, W.-P., BOERSMA, B. J. & UITTENBOGAARD, R. E. 2006 The influence of wall permeability on turbulent channel flow. *J. Fluid Mech.* **562**, 35–72.

BREUGEM, W. P., VAN DIJK, V. & DELFOS, R. 2014 Flows through real porous media: X-ray computed tomography, experiments, and numerical simulations. *Trans. ASME J. Fluids Engng* **136** (4), 040902.

CABAL, A., SZUMBARSKI, J. & FLORYAN, J. M. 2002 Stability of flow in a wavy channel. *J. Fluid Mech.* **457**, 191–212.

CLIFT, R., GRACE, J. R. & WEBER, M. E. 2005 *Bubbles, Drops, and Particles*. Courier Corporation.

COSTA, P., BOERSMA, B. J., WESTERWEEL, J. & BREUGEM, W.-P. 2015 Collision model for fully resolved simulations of flows laden with finite-size particles. *Phys. Rev.* E **92** (5), 053012.

COSTA, P., PICANO, F., BRANDT, L. & BREUGEM, W.-P. 2016 Universal scaling laws for dense particle suspensions in turbulent wall-bounded flows. *Phys. Rev. Lett.* **117** (13), 134501.

COSTA, P., PICANO, F., BRANDT, L. & BREUGEM, W.-P. 2018 Effects of the finite particle size in turbulent wall-bounded flows of dense suspensions. *J. Fluid Mech.* **843**, 450–478.

DE VITA, F., ROSTI, M. E., CASERTA, S. & BRANDT, L. 2019 Numerical simulations of vorticity banding of emulsions in shear flows. arXiv:1902.05448.

DRAZIN, P. G. & REID, W. H. 2004 *Hydrodynamic Stability*. Cambridge University Press.

ESHGHINEJADFARD, A., HOSSEINI, S. A. & THÉVENIN, D. 2017 Fully-resolved prolate spheroids in turbulent channel flows: A lattice Boltzmann study. *AIP Advances* **7** (9), 095007.

FINNIGAN, J. 2000 Turbulence in plant canopies. *Annu. Rev. Fluid Mech.* **32** (1), 519–571.

FREUND, J. B. 2014 Numerical simulation of flowing blood cells. *Annu. Rev. Fluid Mech.* **46**, 67–95.

GUALTIERI, P., BATTISTA, F. & CASCIOLA, C. M. 2017 Turbulence modulation in heavy-loaded suspensions of tiny particles. *Phys. Rev. Fluids* **2** (3), 034304.

GUAZZELLI, E. & MORRIS, J. F. 2011 *A Physical Introduction to Suspension Dynamics*, vol. 45. Cambridge University Press.

HIRT, C. W. & NICHOLS, B. D. 1981 Volume of fluid (VOF) method for the dynamics of free boundaries. *J. Comput. Phys.* **39** (1), 201–225.

IZBASSAROV, D., ROSTI, M. E., ARDEKANI, M. N., SARABIAN, M., HORMOZI, S., BRANDT, L. & TAMMISOLA, O. 2018 Computational modeling of multiphase viscoelastic and elasto-viscoplastic flows. *Intl J. Numer. Meth. Fluids* **88**, 521–543.

JACKSON, P. S. 1981 On the displacement height in the logarithmic velocity profile. *J. Fluid Mech.* **111**, 15–25.

JEFFREY, D. J. 1982 Low-Reynolds-number flow between converging spheres. *Mathematika* **29**, 58–66.

JIMÉNEZ, J., UHLMANN, M., PINELLI, A. & KAWAHARA, G. 2001 Turbulent shear flow over active and passive porous surfaces. *J. Fluid Mech.* **442**, 89–117.

KAJISHIMA, T., TAKIGUCHI, S., HAMASAKI, H. & MIYAKE, Y. 2001 Turbulence structure of particle-laden flow in a vertical plane channel due to vortex shedding. *JSME Intl J.* **44** (4), 526–535.

KIM, J., MOIN, P. & MOSER, R. 1987 Turbulence statistics in fully developed channel flow at low Reynolds number. *J. Fluid Mech.* **177**, 133–166.

KRINDEL, P. & SILBERBERG, A. 1979 Flow through gel-walled tubes. *J. Colloid Interface Sci.* **71** (1), 39–50.

KROGSTADT, P. & ANTONIA, R. A. 1999 Surface roughness effects in turbulent boundary layers. *Exp. Fluids* **27** (5), 450–460.

KUMARAN, V. 1995 Stability of the flow of a fluid through a flexible tube at high Reynolds number. *J. Fluid Mech.* **302**, 117–139.

KUMARAN, V. 1998*a* Stability of the flow of a fluid through a flexible tube at intermediate Reynolds number. *J. Fluid Mech.* **357**, 123–140.

KUMARAN, V. 1998*b* Stability of wall modes in a flexible tube. *J. Fluid Mech.* **362**, 1–15.

KUMARAN, V. & MURALIKRISHNAN, R. 2000 Spontaneous growth of fluctuations in the viscous flow of a fluid past a soft interface. *Phys. Rev. Lett.* **84** (15), 3310.

LAHAV, J., ELIEZER, N. & SILBERBERG, A. 1973 Gel-walled cylindrical channels as models for the microcirculation: dynamics of flow. *Biorheology* **10** (4), 595–604.

LASHGARI, I., PICANO, F., BREUGEM, W. P. & BRANDT, L. 2014 Laminar, turbulent, and inertial shear-thickening regimes in channel flow of neutrally buoyant particle suspensions. *Phys. Rev. Lett.* **113** (25), 254502.

LASHGARI, I., PICANO, F., BREUGEM, W. P. & BRANDT, L. 2016 Channel flow of rigid sphere suspensions: particle dynamics in the inertial regime. *Intl J. Multiphase Flow* **78**, 12–24.

LEE, M. J., KIM, J. & MOIN, P. 1990 Structure of turbulence at high shear rate. *J. Fluid Mech.* **216**, 561–583.

LEONARDI, S., ORLANDI, P., DJENIDI, L. & ANTONIA, R. A. 2004 Structure of turbulent channel flow with square bars on one wall. *Intl J. Heat Fluid Flow* **25** (3), 384–392.

LEONARDI, S., ORLANDI, P., SMALLEY, R. J., DJENIDI, L. & ANTONIA, R. A. 2003 Direct numerical simulations of turbulent channel flow with transverse square bars on one wall. *J. Fluid Mech.* **491**, 229–238.

LOISEL, V., ABBAS, M., MASBERNAT, O. & CLIMENT, E. 2013 The effect of neutrally buoyant finite-size particles on channel flows in the laminar-turbulent transition regime. *Phys. Fluids* **25** (12), 123304.

LUCCI, F., FERRANTE, A. & ELGHOBASHI, S. 2010 Modulation of isotropic turbulence by particles of Taylor length-scale size. *J. Fluid Mech.* **650**, 5–55.

LUNDELL, F., SÖDERBERG, L. D. & ALFREDSSON, P. H. 2011 Fluid mechanics of papermaking. *Annu. Rev. Fluid Mech.* **43**, 195–217.

LUO, H. & BEWLEY, T. R. 2003 Design, modeling, and optimization of compliant tensegrity fabrics for the reduction of turbulent skin friction. In *Smart Structures and Materials 2003: Modeling, Signal Processing, and Control*, vol. 5049, pp. 460–471. International Society for Optics and Photonics.

LUO, H. & BEWLEY, T. R. 2005 Accurate simulation of near-wall turbulence over a compliant tensegrity fabric. In *Smart Structures and Materials 2005: Modeling, Signal Processing, and Control*, vol. 5757, pp. 184–198. International Society for Optics and Photonics.

MATAS, J. P., MORRIS, J. F. & GUAZZELLI, E. 2003 Transition to turbulence in particulate pipe flow. *Phys. Rev. Lett.* **90** (1), 014501.

McKinney, W. & DeLaurier, J. 1981 Wingmill: an oscillating-wing windmill. *J. Energy* **5** (2), 109–115.

Mehta, A. J. 2014 *An Introduction to Hydraulics of Fine Sediment Transport*. World Scientific.

Min, T., Yoo, J. Y. & Choi, H. 2001 Effect of spatial discretization schemes on numerical solutions of viscoelastic fluid flows. *J. Non-Newtonian Fluid Mech.* **100** (1-3), 27–47.

Naso, A. & Prosperetti, A. 2010 The interaction between a solid particle and a turbulent flow. *New J. Phys.* **12** (3), 033040.

Nikuradse, J. 1933 Stromungsgcsetzc in rauhen Rohren, Forschungshefte, 361, VDI. *NACA Tech Mem* 1292.

Nikuradse, J. 1950 *Laws of flow in rough pipes*. National Advisory Committee for Aeronautics Washington.

Orlandi, P. & Leonardi, S. 2008 Direct numerical simulation of three-dimensional turbulent rough channels: parameterization and flow physics. *J. Fluid Mech.* **606**, 399–415.

Pan, Y. & Banerjee, S. 1996 Numerical simulation of particle interactions with wall turbulence. *Phys. Fluids* **8** (10), 2733–2755.

Perot, B. & Moin, P. 1995*a* Shear-free turbulent boundary layers. Part 1. Physical insights into near-wall turbulence. *J. Fluid Mech.* **295**, 199–227.

Perot, B. & Moin, P. 1995*b* Shear-free turbulent boundary layers. Part 2. New concepts for Reynolds stress transport equation modelling of inhomogeneous flows. *J. Fluid Mech.* **295**, 229–245.

Picano, F., Breugem, W. P. & Brandt, L. 2015 Turbulent channel flow of dense suspensions of neutrally buoyant spheres. *J. Fluid Mech.* **764**, 463–487.

Pope, S. B. 2000 *Turbulent Flows*. Cambridge University Press.

Quintard, M. & Whitaker, S. 1994 Transport in ordered and disordered porous media II: Generalized volume averaging. *Transp. Porous Med.* **14** (2), 179–206.

Rallabandi, B., Saintyves, B., Jules, T., Salez, T., Schönecker, C., Mahadevan, L. & Stone, H. A. 2017 Rotation of an immersed cylinder sliding near a thin elastic coating. *Phys. Rev. Fluids* **2** (7), 074102.

Raupach, M. R., Antonia, R. A. & Rajagopalan, S. 1991 Rough-wall turbulent boundary layers. *Appl. Mech. Rev.* **44** (1), 1–25.

Roma, A. M., Peskin, C. S. & Berger, M. J. 1999 An adaptive version of the immersed boundary method. *J. Comput. Phys.* **153** (2), 509–534.

Rosti, M. E. & Brandt, L. 2017 Numerical simulation of turbulent channel flow over a viscous hyper-elastic wall. *J. Fluid Mech.* **830**, 708–735.

Rosti, M. E. & Brandt, L. 2018 Suspensions of deformable particles in a Couette flow. *J. Non-Newtonian Fluid Mech.* **262** (C), 3–11.

Rosti, M. E., Brandt, L. & Mitra, D. 2018*a* Rheology of suspensions of viscoelastic spheres: Deformability as an effective volume fraction. *Phys. Rev. Fluids* **3** (1), 012301(R).

Rosti, M. E., Brandt, L. & Pinelli, A. 2018*b* Turbulent channel flow over an anisotropic porous wall – drag increase and reduction. *J. Fluid Mech.* **842**, 381–394.

Rosti, M. E., Cortelezzi, L. & Quadrio, M. 2015 Direct numerical simulation of turbulent channel flow over porous walls. *J. Fluid Mech.* **784**, 396–442.

Saintyves, B., Jules, T., Salez, T. & Mahadevan, L. 2016 Self-sustained lift and low friction via soft lubrication. *Proc. Natl Acad. Sci. USA* **113** (21), 5847–5849.

Salez, T. & Mahadevan, L. 2015 Elastohydrodynamics of a sliding, spinning and sedimenting cylinder near a soft wall. *J. Fluid Mech.* **779**, 181–196.

Samanta, A., Vinuesa, R., Lashgari, I., Schlatter, P. & Brandt, L. 2015 Enhanced secondary motion of the turbulent flow through a porous square duct. *J. Fluid Mech.* **784**, 681–693.

Shankar, V. & Kumaran, V. 1999 Stability of non-parabolic flow in a flexible tube. *J. Fluid Mech.* **395**, 211–236.

Shao, X., Wu, T. & Yu, Z. 2012 Fully resolved numerical simulation of particle-laden turbulent flow in a horizontal channel at a low reynolds number. *J. Fluid Mech.* **693**, 319–344.

Skotheim, J. M. & Mahadevan, L. 2004 Soft lubrication. *Phys. Rev. Lett.* **92** (24), 245509.

Srivatsan, L. & Kumaran, V. 1997 Flow induced instability of the interface between a fluid and a gel. *J. Phys. II* **7** (6), 947–963.

SUGA, K., MATSUMURA, Y., ASHITAKA, Y., TOMINAGA, S. & KANEDA, M. 2010 Effects of wall permeability on turbulence. *Intl J. Heat Fluid Flow* **31** (6), 974–984.

SUGIYAMA, K., II, S., TAKEUCHI, S., TAKAGI, S. & MATSUMOTO, Y. 2011 A full Eulerian finite difference approach for solving fluid–structure coupling problems. *J. Comput. Phys.* **230** (3), 596–627.

TANAKA, M. & TERAMOTO, D. 2015 Modulation of homogeneous shear turbulence laden with finite-size particles. *J. Turbul.* **16** (10), 979–1010.

TILTON, N. & CORTELEZZI, L. 2006 The destabilizing effects of wall permeability in channel flows: A linear stability analysis. *Phys. Fluids* **18** (5), 051702.

TRYGGVASON, G., SUSSMAN, M. & HUSSAINI, M. Y. 2007 Immersed boundary methods for fluid interfaces. In *Computational Methods for Multiphase Flow*, chap. 3. Cambridge University Press.

UHLMANN, M. 2005 An immersed boundary method with direct forcing for simulation of particulate flow. *J. Comput. Phys.* **209** (2), 448–476.

VREMAN, A. W. 2015 Turbulence attenuation in particle-laden flow in smooth and rough channels. *J. Fluid Mech.* **773**, 103–136.

WANG, G., ABBAS, M. & CLIMENT, E. 2018 Modulation of the regeneration cycle by neutrally buoyant finite-size particles. *J. Fluid Mech.* **852**, 257–282.

YU, Z., WU, T., SHAO, X. & LIN, J. 2013 Numerical studies of the effects of large neutrally buoyant particles on the flow instability and transition to turbulence in pipe flow. *Phys. Fluids* **25** (4), 043305.

ZHANG, Q. & PROSPERETTI, A. 2010 Physics-based analysis of the hydrodynamic stress in a fluid-particle system. *Phys. Fluids* **22** (3), 033306.

ZHOU, J., ADRIAN, R. J., BALACHANDAR, S. & KENDALL, T. M. 1999 Mechanisms for generating coherent packets of hairpin vortices in channel flow. *J. Fluid Mech.* **387**, 353–396.

ZHU, W., VAN HOUT, R. & KATZ, J. 2007 PIV measurements in the atmospheric boundary layer within and above a mature corn canopy. Part II: Quadrant-hole analysis. *J. Atmos. Sci.* **64** (8), 2825–2838.